Low-frequency Faraday rotation measures towards pulsars using LOFAR: probing the 3-D Galactic halo magnetic field

C. Sobey[1,2,3]⋆, A. V. Bilous[4], J-M. Grießmeier[5,6], J. W. T. Hessels[3,4],
A. Karastergiou[7,8,9], E. F. Keane[10], V. I. Kondratiev[3,11], M. Kramer[12], D. Michilli[4,3,13,14],
A. Noutsos[12], M. Pilia[15], E. J. Polzin[16], B. W. Stappers[16], C. M. Tan[16],
J. van Leeuwen[3], J. P. W. Verbiest[17,12], P. Weltevrede[16], G. Heald[2], M. I. R. Alves[18],
E. Carretti[19], T. Enßlin[20], M. Haverkorn[18], M. Iacobelli[3], W. Reich[12], C. Van Eck[21]

[1]*International Centre for Radio Astronomy Research - Curtin University, GPO Box U1987, Perth, WA 6845, Australia*
[2]*CSIRO Astronomy and Space Science, PO Box 1130 Bentley, WA 6102, Australia*
[3]*ASTRON, Netherlands Institute for Radio Astronomy, Oude Hoogeveensedijk 4, 7991 PD, Dwingeloo, The Netherlands*
[4]*Anton Pannekoek Institute for Astronomy, University of Amsterdam, Science Park 904, 1098 XH, Amsterdam, The Netherlands*
[5]*LPC2E - Université d'Orléans / CNRS, 45071 Orléans cedex 2, France*
[6]*Station de Radioastronomie de Nançay, Observatoire de Paris, PSL Research University, CNRS, Univ. Orléans, OSUC, 18330 Nançay, France*
[7]*Oxford Astrophysics, Denys Wilkinson Building, Keble Road, Oxford OX1 3RH, UK*
[8]*Department of Physics & Astronomy, University of the Western Cape, Private Bag X17, Bellville 7535, South Africa*
[9]*Department of Physics and Electronics, Rhodes University, PO Box 94, Grahamstown 6140, South Africa*
[10]*SKA Organisation, Jodrell Bank Observatory, SK11 9DL, UK*
[11]*Astro Space Centre, Lebedev Physical Institute, Russian Academy of Sciences, Profsoyuznaya Str. 84/32, Moscow 117997, Russia*
[12]*Max Planck Institute for Radio Astronomy, Auf dem Hügel 69, 53121 Bonn, Germany*
[13]*Department of Physics, McGill University, 3600 University Street, Montréal, QC H3A 2T8, Canada*
[14]*McGill Space Institute, McGill University, 3550 University Street, Montréal, QC H3A 2A7, Canada*
[15]*INAF - Osservatorio Astronomico di Cagliari, via della Scienza 5, I-09047 Selargius (CA), Italy*
[16]*Jodrell Bank Centre for Astrophysics, School of Physics and Astronomy, The University of Manchester, Manchester, M13 9PL, UK*
[17]*Fakultät für Physik, Universität Bielefeld, Postfach 100131, 33501 Bielefeld, Germany*
[18]*Department of Astrophysics/IMAPP, Radboud University Nijmegen, PO Box 9010, 6500 GL Nijmegen, The Netherlands*
[19]*INAF - Istituto di Radioastronomia, Via Gobetti 101, 40129 Bologna, Italy*
[20]*Max Planck Institut für Astrophysik, Karl-Schwarzschild-Str 1, D-85740 Garching, Germany*
[21]*Dunlap Institute for Astronomy and Astrophysics, University of Toronto, 50 St. George Street, Toronto, ON M5S 3H4, Canada*

ABSTRACT

We determined Faraday rotation measures (RMs) towards 137 pulsars in the northern sky, using Low-Frequency Array (LOFAR) observations at 110–190 MHz. This low-frequency RM catalogue, the largest to date, improves the precision of existing RM measurements on average by a factor of 20 – due to the low frequency and wide bandwidth of the data, aided by the RM synthesis method. We report RMs towards 25 pulsars for the first time. The RMs were corrected for ionospheric Faraday rotation to increase the accuracy of our catalogue to ≈0.1 rad m^{-2}. The ionospheric RM correction is currently the largest contributor to the measurement uncertainty. In addition, we find that the Faraday dispersion functions towards pulsars are extremely Faraday thin – mostly less than 0.001 rad m^{-2}. We use these new precise RM measurements (in combination with existing RMs, dispersion measures, and distance estimates) to estimate the scale height of the Galactic halo magnetic field: 2.0±0.3 kpc for Galactic quadrants I and II above and below the Galactic plane (we also evaluate the scale height for these regions individually). Overall, our initial low-frequency catalogue provides valuable information about the 3-D structure of the Galactic magnetic field.

Key words: pulsars: general – techniques: polarimetric – radio telescopes – ISM: magnetic fields – Galaxy: structure

arXiv:1901.07738v1 [astro-ph.GA] 23 Jan 2019

1 INTRODUCTION

Magnetic fields are ubiquitous in the Universe. They play a role in numerous astrophysical processes across a range of physical scales and field strengths. Within galaxies, magnetic fields pervade the multi-phase diffuse interstellar medium (ISM).

Galactic magnetic fields can be modelled as a combination of a large, kiloparsec-scale, coherent component; a component with a power spectrum of small-scale (1–100 parsec), random fluctuations; and an intermediate-scale component that is ordered overall but with small-scale field direction reversals (e.g. Jaffe et al. 2010). The coherent component observed, for example, in 'magnetic spiral arms' (e.g. Beck 2009) accelerates and confines cosmic rays (e.g. Aharonian et al. 2012, and references therein) and may be maintained by a turbulent dynamo (e.g. Dobbs et al. 2016). The random component, caused by turbulence, supernovae and shocks, and other localised phenomena (e.g. Haverkorn et al. 2015) plays a role in, for example, the formation of molecular clouds and stars (e.g. Crutcher 2012). The intermediate ordered component is thought to result from larger-scale effects, including shearing dynamics and compression, on the random component (e.g. Jaffe et al. 2010) and plays a role in, for example, the transport of heat and angular momentum (e.g. Haverkorn 2015). In the Milky Way, the random and ordered components can be between 0.5- and 5-times the magnitude of the coherent component, depending on the observables (see below), regions studied, and assumptions used (e.g. Rand & Kulkarni 1989; Haverkorn et al. 2004, 2006; Schnitzeler et al. 2007; Jaffe et al. 2010, 2011; Beck et al. 2016).

The (magnetic) structure of our Galaxy is challenging to study because we are embedded within it. The Galactic magnetic field (GMF) was first measured over 65 years ago using polarisation of starlight (Hall 1949; Hiltner 1949). There are several other observables that provide information about the GMF, including Zeeman splitting of spectral lines (e.g. Crutcher et al. 2010); polarised thermal emission from dust grains (e.g. Planck Collaboration et al. 2016); total intensity and polarisation of Galactic synchrotron emission (e.g. Sun et al. 2008); Faraday rotation of polarised sources (e.g. Van Eck et al. 2011); and ultra-high energy cosmic rays (e.g. Farrar et al. 2013). These observables (mostly 2-D tracers requiring ancillary data) usually provide information about the strength/direction of at least one component of the magnetic field parallel/perpendicular to the line-of-sight (LoS) within a particular phase of the ISM (e.g. Ferrière 2011; Haverkorn 2015). Several of these observables will be required to accurately reconstruct the multiple-scale components of the GMF (e.g. Jaffe et al. 2010; Boulanger et al. 2018).

Our current picture of the large-scale GMF is that the field strength is on the order of $\sim$2–10 μG; $\approx$2 μG at the solar position and increasing towards the Galactic centre and decreasing towards the anticentre (e.g. Beck 2001; Brown et al. 2003; Han et al. 2006). Recent analyses of the large-scale disc component often favour an axisymmetric spiral with an overall clockwise direction (as viewed from the north Galactic pole) that seems to somewhat follow the spiral-arm structure, with one field direction reversal near the Sun in the direction of the Galactic centre along the Scutum-Centaurus

arm (e.g. Van Eck et al. 2011; Jansson & Farrar 2012). However, the total number and locations of the large-scale GMF reversals are still under debate (e.g. Han et al. 2006), and many open questions concerning the 3-D structure of the aggregate GMF (along with its generation and evolution) remain (e.g. Ferrière 2011). Furthermore, such reversals have not yet been observed in any other galaxies (e.g. Beck et al. 2015). Another component of the large-scale GMF often considered separately to the disc, is the halo (absolute Galactic latitude greater than a few degrees, e.g., Han et al. 2018). The 3-D GMF structure in the halo is less well understood, with several proposed geometries (see, e.g., Haverkorn 2015; Terral & Ferrière 2017, and references therein), including a north–south asymmetry across the Galactic disc (Mao et al. 2012). Despite the challenges, our Galaxy also provides a unique opportunity to study the magnetic field structure at much smaller scales, essential for comparison with nearby galaxies (e.g. Nota & Katgert 2010).

Faraday rotation measurements of polarised radio sources have been used to measure the magnetic field strength and direction in the intervening (warm) ISM parallel to the LoS. This method has been used to investigate the structure of the GMF by using a large sample of sources, including pulsars (e.g. Manchester 1972, 1974; Rand & Lyne 1994; Han et al. 1999, 2006; Noutsos et al. 2008), extragalactic sources (e.g. Mao et al. 2010; Oppermann et al. 2012, 2015), and a combination of both (e.g. Brown et al. 2007; Van Eck et al. 2011). Polarisation observations of a large set of pulsars can be used to probe the 3-D structure of the GMF efficiently. The ratio between the Faraday rotation measure (RM) and the dispersion measure (DM) towards a pulsar at distance d (pc) provides an estimate of the electron density-weighted average magnetic field strength and net direction parallel to the LoS:

$$\langle B_\parallel \rangle = \frac{\int_0^d n_e B_\parallel \mathrm{d}l}{\int_0^d n_e \mathrm{d}l} = 1.232 \ \mu\text{G} \left(\frac{\text{RM}}{\text{rad m}^{-2}}\right)\left(\frac{\text{DM}}{\text{pc cm}^{-3}}\right)^{-1}, \quad (1)$$

where n_e is the electron density and $\mathrm{d}l$ is the differential distance element. By definition, positive (negative) RMs indicate that the net direction of $\langle B_\parallel \rangle$ is towards (away from) the observer. Equation 1 assumes that the electron density and magnetic field are uncorrelated (e.g. Beck et al. 2003). Furthermore, pulsar emission is often highly (linearly) polarised (e.g. Johnston & Kerr 2018), and Faraday rotation internal to the pulsar magnetosphere is negligible (e.g. Wang et al. 2011), facilitating measurement of the RM due to the foreground ISM alone. Thus, it is also expected that pulsars are 'Faraday thin' point sources, where the polarised flux detected lies at a single Faraday depth (i.e. the RM dispersion is negligible; in contrast to a Faraday thick source with polarised flux distributed over a range of Faraday depths). There are 2659 known pulsars[1] distributed throughout the Galaxy, particularly near the disc (Manchester et al. 2005). Currently, 1133 pulsars (43 per cent) have published RMs – two-thirds of which are located in the Southern sky, near the Galactic plane, and are mostly concentrated within a few kiloparsecs from the Sun (Manchester et al. 2005). The

---

[1] Current version of pulsar catalogue (1.59) retrieved from http://www.atnf.csiro.au/people/pulsar/psrcat/

mode RM measurement in the pulsar catalogue was taken at the Parkes Observatory at a frequency of $\approx 1.4\,\mathrm{GHz}$, using 128 MHz bandwidth (e.g. Han et al. 2006; Noutsos et al. 2008; Han et al. 2018). Pulsar distances are estimated using their DMs and a model of the Galactic thermal electron density, e.g., TC93 (Taylor & Cordes 1993); NE2001 (Cordes & Lazio 2002); YMW16 (Yao et al. 2017). However, these distance estimates can be quite uncertain, and only ≈ 200 pulsars have independent distance measurements (e.g. Yao et al. 2017; Deller et al. 2018). Therefore, it is possible that what are interpreted as field reversals along spiral arms may be caused by other intermediate-scale structures, e.g., superbubbles (Haverkorn 2015). RMs measured towards extragalactic sources provide complementary information about the integrated LoS through (at least) the Galaxy, which partially smooths out smaller scale structure.

Work towards better understanding astrophysical magnetic fields, including the GMF, is ongoing. The recent construction of low-frequency (<300 MHz), next-generation aperture array telescopes (and their associated supercomputing facilities) has rejuvenated this field. These include the Low-Frequency Array (LOFAR; van Haarlem et al. 2013) and the Long-Wavelength Array (LWA; Taylor et al. 2012) in the Northern Hemisphere, and the Murchison Widefield Array (MWA; Tingay et al. 2013) in the Southern Hemisphere. Polarisation observations from low-frequency telescopes such as these are providing precise measurements of ISM parameters, due to the wavelength-squared dependencies from the effects of dispersion and Faraday rotation (e.g. Stovall et al. 2015; Kondratiev et al. 2016; Lenc et al. 2016; Van Eck et al. 2017). These facilities are the pathfinders or the precursor to the low-frequency aperture array component of the Square Kilometre Array (SKA-Low), which will operate at 50–350 MHz (Keane 2018). The SKA's capabilities for pulsar discoveries, timing, and astrometry will revolutionise radio astronomy and will be invaluable for studying the GMF in 3-D on large and small scales (e.g. Han et al. 2015).

In this paper, we present RM measurements towards 137 pulsars using low-frequency (<200 MHz) polarisation observations from the 'LOFAR census of non-recycled pulsars' (Bilous et al. 2016) and the 'LOFAR census of millisecond pulsars' (Kondratiev et al. 2016). This also includes RM measurements towards PSR B0329+54, using several LOFAR (timing/monitoring) observations to further investigate the accuracy of the current ionospheric RM correction method. This is the largest low-frequency RM catalogue to date and is also the first to report a large number of RM dispersion measurements for pulsars. These measurements are complementary to similar low-frequency RM catalogues towards extragalactic sources that trace LoSs through (at least) the entire Galaxy (e.g. Neld et al. 2018; Van Eck et al. 2018; Riseley et al. 2018), as well as polarisation observations of diffuse Galactic synchrotron emission that traces the GMF in the plane of the sky (e.g. Jelić et al. 2015; Van Eck et al. 2017). We aim to increase the number of pulsars with RM data and provide higher-precision RM measurements for those already in the literature, to study the large-scale structure of the GMF in the Galactic halo. These data also provide a baseline measurement towards monitoring fluctuations in RM over time to investigate the small-scale magneto-ionic structure in the ISM in the future.

The LOFAR observations and data reduction are described in Section 2. In Section 3 we present a summary of our catalogue of low-frequency DMs and RMs. In Section 4 we discuss our results, including an estimate of the scale height of the Galactic halo magnetic field, and address the limitations of the current data and methods. We provide a summary and our conclusions in Section 5. Appendix A presents the table of LOFAR RM and RM dispersion measurements, and Appendix B presents further details of the RM-synthesis analysis and the Faraday dispersion functions (FDFs or Faraday spectra) obtained for each pulsar with a significant RM detection.

2 OBSERVATIONS AND DATA REDUCTION

All of the observations were performed using LOFAR, which can observe the northern sky between 10–90 and 110–240 MHz (for a description of LOFAR see van Haarlem et al. 2013). The large instantaneous bandwidth available (up to 96 MHz) and large collecting area (up to 24 core stations in the tied-array mode) provide high-quality polarisation data at low frequencies that are well-suited to measuring precise RMs (e.g. Noutsos et al. 2015). The LOFAR observations of pulsars presented in this paper were conducted between 2012 December and 2014 November, with a typical integration time of $\geqslant 20$ min, using the observations summarised in Bilous et al. (2016) and Kondratiev et al. (2016).

The signals received from between 20 and 24 of the LOFAR High-Band-Antenna (HBA) core stations were coherently combined, using the single distributed clock signal and the LOFAR correlator/beam-former, to establish a tied-array beam (for a description of LOFAR's pulsar observing modes see Stappers et al. 2011). The pulsar observations were recorded at a centre frequency of 148.9 MHz, with 78.1 MHz of contiguous bandwidth using the eight-bit sampling mode. The data from the observations were recorded in one of two formats. For the millisecond pulsars (MSPs), the raw complex-voltage (CV) data were recorded with a sampling time of 5.12 μs and a channel width of 195.3 kHz, allowing the data to be coherently dedispersed (e.g. Kondratiev et al. 2016). For the slower non-recycled pulsars with larger rotational periods (allowing larger sampling times and incoherent dedispersion, resulting in smaller data volume), the Stokes *IQUV* parameters were computed and recorded with a sampling time $(1–8) \times 163.8$ μs and each 195.3 kHz sub-band was split into an additional $(1–8) \times 32$ channels (e.g. Bilous et al. 2016).

The recorded data were pre-processed using the LOFAR PULsar Pipeline (PULP, a Python-based suite of scripts that provides basic offline pulsar processing; Kondratiev et al. 2016). The dedispersion and folding were performed using each pulsar's timing ephemeris obtained from Jodrell Bank Observatory or the Green Bank Telescope where available (e.g. Pilia et al. 2016; Bilous et al. 2016), or the pulsar catalogue. The dedispersion and folding were performed on each frequency channel using the DSPSR[2] digital signal-processing software (van Straten & Bailes 2011) and written as a PSRFITS[3] archive (Hotan et al. 2004). The folding pro-

---

[2] http://dspsr.sourceforge.net
[3] http://www.atnf.csiro.au/research/pulsar/psrfits/

duced sub-integrations of between 5 s and 1 min. Radio frequency interference (RFI) in the data was initially removed in affected frequency subbands and time subintegrations using automated programs, i.e., PAZ from the PSRCHIVE[4] software suite (Hotan et al. 2004), and CLEAN.PY from the COASTGUARD[5] software suite (Lazarus et al. 2016). The archives were averaged in frequency to 400 channels and stored in the LOFAR Long-Term Archive[6]. The optimal DM and period (P) of the pulsars were determined previously (Bilous et al. 2016; Kondratiev et al. 2016). The data were inspected to excise obvious remaining RFI using the interactive PSRCHIVE PAZI program. Table 1 shows a summary of the observational and corresponding RM-synthesis parameters, see Section 2.1.

The data have not yet been polarisation calibrated, to account for the parallactic angle or the tied-array instrument beam. The polarisation calibration will be implemented in future work, which will also present the average polarisation profiles of the data described here. For aperture arrays, including LOFAR, polarisation calibration is non-trivial. There are no wavelength-squared-dependent variables in LOFAR's beam response model, especially very close to the pointing centre (where all of the observed pulsars were located), and the parallactic angle is independent of frequency (e.g. Noutsos et al. 2015), leaving the Faraday rotation signal in the data unaffected. Using observations of nine of the pulsars in this work, we verified that the RMs determined before the current polarisation calibration pipeline are equal to those post-calibration. Moreover, the low-frequency data from LOFAR provide a wide bandwidth, throughout which even low RM values cause the Stokes Q, U parameters to vary over many sinusoidal cycles. For example, a small RM of just 1 rad m^{-2} causes the Stokes Q, U parameters to undergo over 1.5 sinusoidal cycles across the 110–190 MHz recorded bandwidth range. Therefore, the Faraday rotation effect that causes the sinusoidal variation in the Stokes Q, U signal with wavelength squared (see Section 2.1) is distinct compared to other possible wavelength-dependant variations due to, e.g., telescope beam effects or pulse profile evolution. LOFAR's X-Y dipoles are rotated 45 degrees away from North, so that when the Stokes parameters are recorded, the RM sign is opposite to the IAU convention (Heald et al. 2018). Therefore, the signs of the RMs measured in this work were flipped to be consistent with the IAU convention used in the pulsar catalogue. The LOFAR beam model corrects this effect, so this sign flip will not be necessary post-polarisation calibration.

Table A1 provides the additional observational parameters (i.e. Modified Julian Date) for each pulsar with a measured RM.

2.1 Determining RMs using RM-synthesis

A polarised wave travelling through a magnetised plasma (such as the ISM) is subject to the effect of Faraday rotation: the polarisation angle, $\chi = 0.5 \tan^{-1}(U/Q)$ (rad), rotates as

a function of the wavelength, λ (m), squared:

$$\chi(\lambda^2) = \chi_0 + \mathrm{RM}\lambda^2, \tag{2}$$

where the RM (rad m^{-2}) characterises the magnitude of the effect, and is dependent on the integrated electron density and magnetic field strength parallel to the LoS, see Equation 1. χ_0 represents the intrinsic polarisation angle of the polarised source's emission.

It has been common practice to measure RMs by determining the gradient of the observed polarisation angle as a function of wavelength squared (e.g. Rand & Lyne 1994). More recently, advancements in computing power have facilitated the recording of larger bandwidths from radio observations and have enabled the use of the powerful method of RM-synthesis (Burn 1966; Brentjens & de Bruyn 2005) for investigating magnetic fields (e.g. Heald et al. 2009; Lenc et al. 2016; Van Eck et al. 2017). This method takes advantage of the Fourier-like relationship between the complex polarisation intensity vector as a function of wavelength squared, $P(\lambda^2) = Q(\lambda^2) + iU(\lambda^2)$, and the Faraday dispersion function (FDF; also referred to as the Faraday spectrum, $F(\phi)$) as a function of Faraday depth, ϕ, advantageously using the entire frequency coverage of the data simultaneously for determining the Faraday depth or RM. Following Brentjens & de Bruyn (2005), the FDF is given by:

$$\tilde{F}(\phi) \approx K \sum_{i=1}^{N} \tilde{P}(\lambda_i^2) e^{-2i\phi(\lambda_i^2 - \lambda_0^2)}, \tag{3}$$

where λ_i is the central wavelength of channel i from the observation; λ_0 is the reference wavelength (ideally the weighted average of λ_i^2); $\tilde{P}(\lambda_i^2) = w_i P(\lambda_i^2) = w_i \left[Q(\lambda_i^2) + iU(\lambda_i^2) \right]$; and K is the inverse sum of all weights w_i. We allowed the weights w_i to be set to an equal value for all observed wavelengths. In the context of this work, RM and ϕ terms can be used interchangeably. Here, we use 'ϕ' in reference to the FDF outputs from RM-synthesis, and 'RM' in reference to the measurements obtained from the FDFs (as well as from the pulsar and extragalactic catalogues). See Figure 1 for the RM spread function (RMSF; analogous to an optical telescope's point spread function, formally RMTF in Brentjens & de Bruyn 2005), showing the theoretical response of the wavelength squared coverage of our LOFAR data in Faraday depth.

For each average LOFAR pulsar profile, the on-pulse Stokes parameters (for each frequency channel) were extracted using the PSRCHIVE RMFIT routine. For profiles with significant signal-to-noise in linear polarisation (where S/N$_P > 7$), the selected on-pulse region was identified as the phase bin with the largest S/N$_P$. Since the profiles were not yet corrected for Faraday rotation, many of the linear polarisation profiles were depolarised, and in these cases (S/N$_P \leqslant 7$) the pulse phase bin with the highest total intensity (Stokes I) was selected as the on-pulse phase bin. We used a small number of on-pulse pulse profile bins to extract the Stokes parameters because this seems to minimise the instrumental polarisation fraction in the data, see below and Appendix B for further discussion.

The Stokes-parameter data were used as the input to a publicly available RM-synthesis program[7], written in


Table 1. Summary of LOFAR HBA data used in this work and corresponding theoretical RM-synthesis parameters.

Parameter	Symbol	Data
Centre frequency	ν	148.9 MHz
Bandwidth	$\Delta\nu$	78.1 MHz
Channel width (averaged)	$\delta\nu$	195 kHz
Centre wavelength squared	λ^2	4.0 m^2
Total bandwidth in wavelength squared ($\lambda^2_{max} - \lambda^2_{min}$)	$\Delta(\lambda^2)$	4.9 (7.4–2.5) m^2
Resolution in Faraday space (FWHM of the RMSF)	$\delta\phi$	0.7 rad m^{-2}
Largest scale in Faraday space to which one is sensitive	max-scale/$\Delta\phi$	1.2 rad m^{-2}
Maximum observable Faraday depth (at $\nu_{min}, \nu, \nu_{max}$, respectively)	$\|\phi_{max}\|$	66,163,327 rad m^{-2}
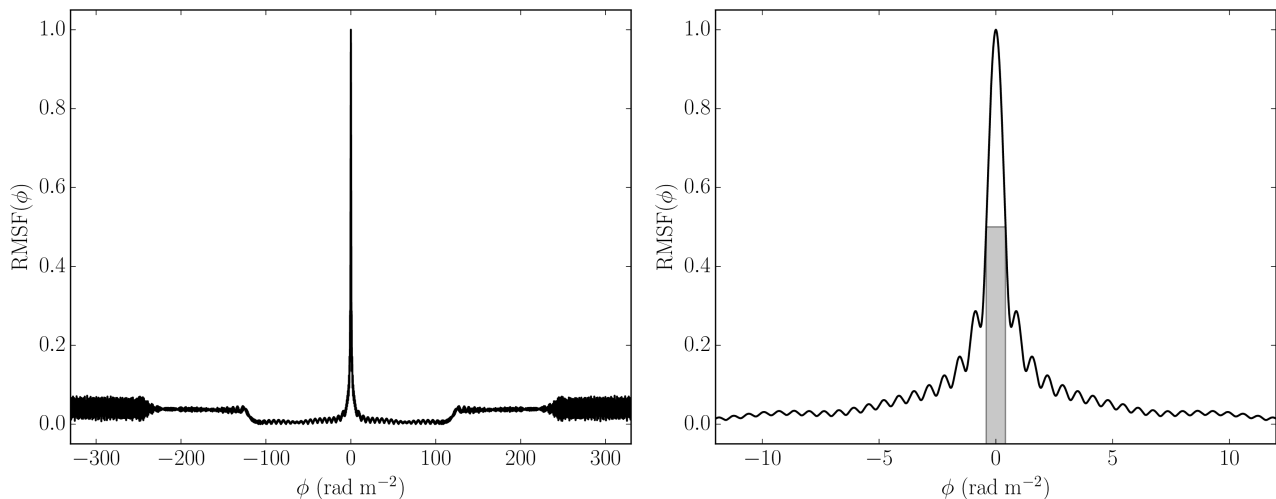
Figure 1. Theoretical, noiseless RMSF expected from RM-synthesis using the LOFAR data parameters summarised in Table 1, shown for both large (left) and narrow (right) ranges in Faraday space. Right: The resolution in Faraday space, $\delta\phi$, is also shown by the FWHM of the RMSF shaded in grey.

PYTHON, which computed the FDF. An example FDF obtained from a LOFAR observation of PSR B0329+54 is shown in Figure 2. The FDFs were computed in the range $-330 \leqslant \phi \leqslant 330$ rad m^{-2} in steps of $\delta\phi = 0.001$ rad m^{-2} to oversample the FDF in Faraday space. The largest RM to which we have more than 50% sensitivity to, at the centre observing frequency, is $|\phi_{max}| = \sqrt{3}/\delta(\lambda^2) = 163$ rad m^{-2}. This quantity is dictated primarily by the observing channel width in wavelength squared $\delta(\lambda^2)$ (Equation 63 from Brentjens & de Bruyn 2005). The RM range of ±330 rad m^{-2} was computed for the FDFs because this is twice the $|\phi_{max}|$ value. This also provided a large range in ϕ with which to calculate the rms noise value. An alternative method for calculating this quantity from Schnitzeler & Lee (2015) gives a somewhat similar expected value of $|\phi_{max}| = 125$ rad m^{-2}. See Table 1 for a summary of the observation and RM-synthesis parameters.

After we obtained an FDF for each pulsar, the location of the peak in Faraday space was determined and fitted using a quadratic function, providing a measurement of the RM. This was regarded as significant if the peak signal-to-noise in the FDF was greater than 4, S/N$_F$ > 4. This threshold was chosen because after conducting RM-synthesis with several examples of noise as the input (i.e. off-pulse data), we found that all of the peaks in the FDFs had a S/N$_F$ $\leqslant$3.8, although the large majority had S/N$_F$ <3.

Any possible instrumental polarisation response around 0 rad m^{-2} (due to no wavelength-squared dependency) was excised from the FDFs. Instrumental polarisation can result from, for example, low levels of RFI that have not been excised in the previous data reduction steps, or from 'leakage', where emission from Stokes I 'leaks' into the other Stokes parameters, causing the mean values of Stokes Q, U to be unequal. Stokes Q is generally most affected by leakage because it is formed from the same polarisation bases as Stokes I. This leakage can somewhat be reduced by polarisation calibrating the data, using a model for the primary beam, for example. However, the beam models and other empirical corrections used for low-frequency aperture-array telescopes such as LOFAR cannot currently completely remove this polarisation leakage (e.g. Lenc et al. 2017). A major advantage in using low-frequency data to obtain RMs is that the FWHM of the RMSF is narrow, enabling identification and separation of the peaks resulting from any instrumental polarisation and the desired astronomical RM signal in the FDF. For the LOFAR data presented in this work, the theoretical FWHM of the RMSF is $\delta\phi = 3.8/\Delta(\lambda^2) \approx 0.7$ rad m^{-2} (Equation 61 in Brentjens & de Bruyn 2005; Schnitzeler et al. 2009). This small value for $\delta\phi$ facilitates the precise measurement of RMs, see Figures 1 and 2. For the FDFs obtained in this work, we excised the signal within $\pm\delta\phi$ around 0 rad m^{-2}, i.e., $-0.7 < \phi < 0.7$ rad m^{-2}. This allows the measurement of absolute RMs above ≈ 0.7 rad m^{-2}, which applies to 99 per cent of the current pulsar catalogue. In addition, the absolute ionospheric RM is often on the order of ≈ 1 rad m^{-2}, see Section 2.2. We measured the location of
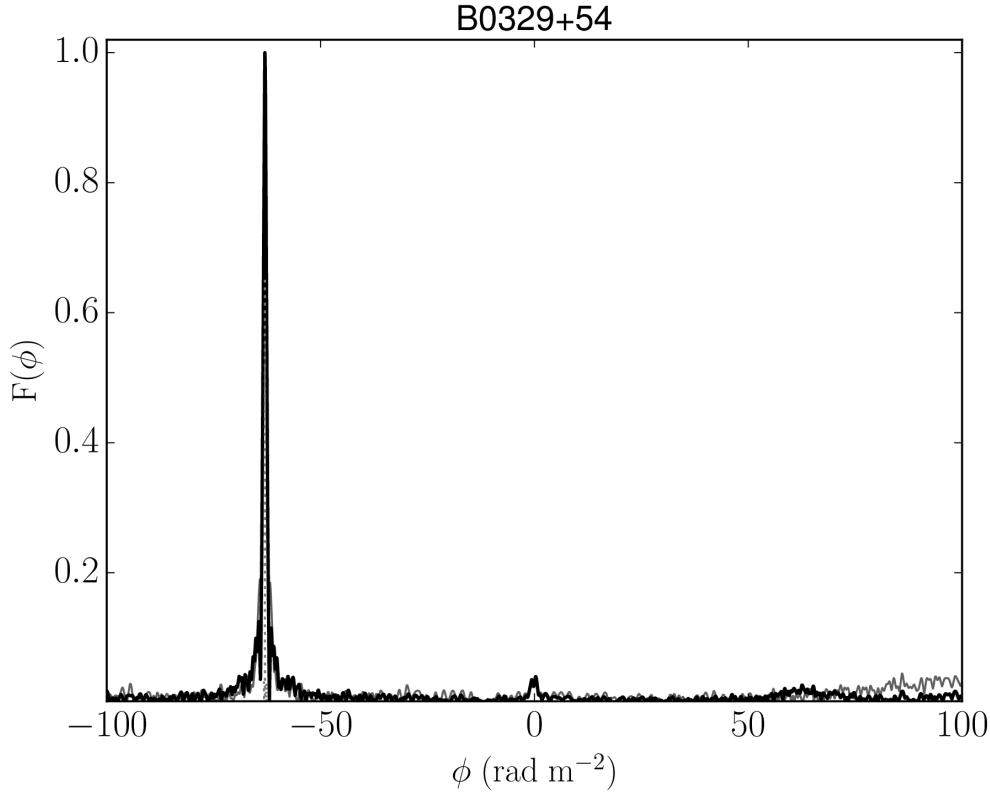
Figure 2. An example Faraday dispersion function (FDF; grey line) using a 10-minute LOFAR HBA observation towards PSR B0329+54 centred at 149 MHz. The vertical axis is in arbitrary units (normalised) because the data are not flux or polarisation calibrated, see text for further details. The black line shows the resulting spectrum produced after ten iterations of RM CLEAN, stopping at the specified $8 \times \mathrm{rms}$ threshold. The dotted grey lines show the locations of the RM CLEAN components centred at $\mathrm{RM_{obs}} = -63.016 \pm 0.005\,\mathrm{rad\,m^{-2}}$, before correcting for the ionospheric RM. A small amount of instrumental polarisation (3 per cent) is evident near $0\,\mathrm{rad\,m^{-2}}$. A small amount of leakage to $+63\,\mathrm{rad\,m^{-2}}$ and some RMSF structure at larger RM values can also be seen in the baseline.

the peak in the FDFs due to the instrumental polarisation near $0\,\mathrm{rad\,m^{-2}}$, and a histogram of the results are shown in Figure B2. We find that the instrumental peaks in the FDFs do not deviate greatly from $0\,\mathrm{rad\,m^{-2}}$.

The formal RM uncertainty was determined by measuring the FWHM of the signal peak in the FDF (i.e. the measured value for $\delta\phi$; FWHM_F), as well as the $\mathrm{S/N}_F$. The rms noise in the FDF was calculated across the search range in RM space, excluding the peak(s) associated with the pulsar signal and the instrumental response near $0\,\mathrm{rad\,m^{-2}}$. The formal RM uncertainty was calculated as

$$\frac{\mathrm{FWHM_F}}{2 \times \mathrm{S/N_F}}, \qquad (4)$$

following Brentjens & de Bruyn (2005); Schnitzeler & Lee (2017).

If no significant peak in the FDF was detected, i.e., $\mathrm{S/N}_F < 4$, attempts to increase the $\mathrm{S/N}_F$ were made by extracting the integrated Stokes parameters for an increasingly large range of the on-pulse phase bins in the average pulse profile, up to the full width at 10 per cent of the maximum of the profile. The total number of phase bins in the pulsar profiles is mostly 1024, but range from 64 to 1024 in powers of 2, and are listed in Table A1. The median number of phase bins used to extract the Stokes parameters was 3 for the 'slow' pulsar census and 8 for the MSP census, these are

also listed for each pulsar in Table A1. The total number of bins summed were increased gradually to minimise possible effects of varying polarisation angle and/or RM across the pulse profile (e.g. Noutsos et al. 2015), which will be investigated in future work. For FDFs with $4 < \mathrm{S/N}_F < 8$, the formal error was multiplied by 2, to reflect the larger uncertainties on the lower S/N detections. This was approximately the deviation in the RMs obtained using a subset of the pulsar data, with multiple ranges in the pulse profile bins to extract the Stokes parameters, see Appendix B for further discussion and Figure B1 for high and low S/N examples. FDFs with $\mathrm{S/N}_F \geqslant 8$ have been shown to be reliable (e.g. George et al. 2012). Although RMs can also be measured as a function of pulse phase space, low-frequency observations indicate much less deviation across the pulse profile compared to higher-frequency data (e.g. Noutsos et al. 2009, 2015). Pulsar observations where between one and five phase bins were used to measure the RMs are good candidates for phase-resolved RM studies in future work.

The RM-synthesis was coupled with RM CLEAN[7] analysis to deconvolve the FDF using the theoretical RMSF (Heald et al. 2009; Michilli et al. 2018c). RM CLEAN allowed us to estimate the intrinsic Faraday spectrum, to obtain the second moment of the RM CLEAN components (RM dispersion; σ_{RM}), and to investigate the extent to which the FDFs obtained are Faraday thin (e.g. Heald et al. 2009;

Anderson et al. 2015). Faraday thickness can originate in volumes of plasmas with regular magnetic fields that both emit and Faraday rotate, or in plasmas with turbulent magnetic fields that Faraday rotate, leading to polarised flux being distributed over a range of Faraday depths (Burn 1966). A Faraday thin source satisfies $\lambda^2 \Delta\phi \ll 1$, where $\Delta\phi$ is the extent of the source in Faraday space (Brentjens & de Bruyn 2005). FDFs calculated from low-frequency data provide the tightest constraint on $\Delta\phi$ because of the large λ^2, which is $4.9 \, \text{m}^2$ for the LOFAR data in this work, see Table 1. The largest scale in Faraday space to which one is sensitive, using these LOFAR data, is $\pi/\lambda_{min}^2 = 1.2 \, \text{rad m}^{-2}$ (Equation 62 in Brentjens & de Bruyn 2005). Pulsars are not expected to be Faraday-resolved (-thick) sources because they are point sources and their magnetospheric emission is not expected to impart Faraday rotation, in particular with the usual wavelength squared dependency, due to the relativistic electron-positron pair plasma expected in their magnetospheres (e.g. Wang et al. 2011). The degree of polarisation emitted often increases towards lower frequencies (e.g. Johnston et al. 2008; Noutsos et al. 2015), which is also contrary to that expected from a Faraday thick source that becomes substantially depolarised towards longer wavelengths. Despite this expectation, the RM dispersion of pulsars has not been widely explored in the literature.

In this work, the polarisation data were normalised by a power-law model characterised by a spectral index, α, that was fitted to the apparent Stokes I spectrum ($S(\nu) \propto \nu^{-\alpha}$). For each pulsar, the FDF was computed and, if a significant RM was detected, we RM CLEANed down to 3×rms of the noise in the FDF. Any peak in the FDF near 0 rad m^{-2} caused by instrumental polarisation was ignored in this analysis.

Using the method described above, a single number for the RM (and RM dispersion) towards each pulsar was obtained for the purpose of studying the GMF, and are summarised in Table A1. All uncertainties are labelled '±' in this paper, to avoid confusion with the RM dispersion, σ_{RM}. Pulsars with published RMs in the pulsar catalogue were cross-checked with the results from this work to verify and compare the (low-frequency) RMs obtained, see Section 3. Future work will present the calibrated polarisation profiles and phase-resolved RMs, in order to further investigate, e.g., the pulsar emission mechanism.

2.2 Ionospheric Faraday rotation subtraction

The ionosphere, also a magneto-ionic plasma, introduces an additional RM that is both time and position dependent. Therefore, the ionospheric RM, RM$_{ion}$, must be subtracted from the observed RM, RM$_{obs}$, in order to obtain a measurement of the RM due to the ISM alone, i.e., RM$_{ISM}$ = RM$_{obs}$–RM$_{ion}$.

The RM$_{ion}$ towards the LoS (at the corresponding ionospheric pierce point, IPP) at the time of each observation was calculated by using a previously tested and verified code, ionFR[8] (see Sotomayor-Beltran et al. 2013). This code models the RM$_{ion}$ using vertical total electron content (VTEC) maps of the ionosphere (obtained using the distribution of

worldwide GPS stations) plus a standard mathematical description of the Earth's main magnetic field. Several pulsar observations taken over the course of several hours have previously been used to investigate the RM$_{ion}$ – estimated using several publicly available VTEC maps[9] as inputs (e.g. Sotomayor-Beltran et al. 2013; Sobey 2015). The CODE (e.g. Dach et al. 2018) and IGS (e.g. Hernández-Pajares et al. 2009) VTEC maps used to produce RM$_{ion}$ estimates were found to provide a good fit to the RM$_{obs}$. In this work, the IGS TEC maps were used because they generally have smaller uncertainties (calculated using the VTEC rms maps), which are the largest contribution to the uncertainty in RM$_{ion}$. For this work, we also updated the ionFR code to use the most recent version of the International Geomagnetic Reference Field[10] (IGRF-12; Thébault et al. 2015). Comparing the ionFR output between using the previous and current versions of the IGRF (11 or 12, respectively), the RM$_{ion}$ values differ by less than 2 per cent of the uncertainties (in the cases of several pulsar LoSs tested). IGRF-12 was used because it is the most recent release and provides the geomagnetic field components beyond the year 2015.

In this work, we also investigated the repeatability of this method for estimating RM$_{ion}$ over a longer timespan ($\approx$year), and the accuracy of the resulting RM$_{ISM}$ measurements that can be expected. Ten (timing/monitoring) observations of a bright, northern pulsar B0329+54, were used to compare the RM$_{obs}$ and RM$_{ion}$ over the course of nine months from 2014 February 3 to 2014 November 3. These observations used the same parameters as those shown in Table 1. We measured the DM for each observation using the pdmp routine in PSRCHIVE and corrected the archive file for this value. We then measured the RM$_{obs}$ using the method described in Section 2.1. We used the IGS VTEC maps and IGRF-12 as inputs to the ionFR code to estimate RM$_{ion}$ for each average observation time (and corresponding IPP) for PSR B0329+54. We do not apply the ionospheric RM correction to the pulsar archive files on timescales shorter than one observation. This is because the data are not severely depolarised over the short integration time (just $\approx$10–20 minutes in length) and the pulsar signals are often highly polarised. Observations could be corrected on shorter timescales, if particularly active ionospheric conditions dictate that this is necessary. However, the IGS VTEC maps we use have a time resolution of 2 hours (interpolated to every hour in the ionFR code) and we find that a single RM$_{ion}$ correction per observation is sufficient for this work. We corrected RM$_{obs}$ using the RM$_{ion}$ values output from ionFR, and also calculated the inferred electron-density-weighted $\langle B_\parallel \rangle$ using Equation 1. The results are shown in Figure 3.

The weighted mean of the DM measurements of PSR B0329+54, shown in Figure 3, is 26.7624 pc cm^{-3} with a standard deviation of 0.0008 pc cm^{-3}. The DM measurements are not corrected for the ionospheric DM because the ionosphere imparts a negligible amount of DM compared to the measurement uncertainties here. Figure 3 shows that the variation in the RM$_{ion}$ estimates appears to be a good fit to that for the RM$_{obs}$ measurements. The weighted mean of

---

[8] https://sourceforge.net/projects/ionfarrot/

[9] available at NASA's Archive of Space Geodesy Data, retrieved from ftp://cddis.nasa.gov/pub/gps/products/ionex/.
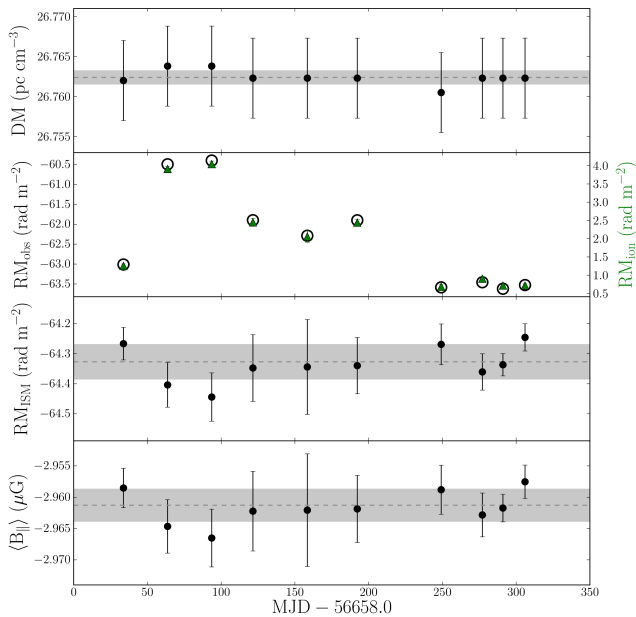[10] https://www.ngdc.noaa.gov/IAGA/vmod/igrf.html

Figure 3. Measurements using the LOFAR timing observations of PSR B0329+54 centred at 149 MHz with 78 MHz bandwidth. From the upper to lower panels we show the following quantities plotted against Modified Julian Date from 2014 January 1 (MJD= 56658): the measured DMs; the observed RMs (RM_{obs}; open circles; left y-axis) and the estimated ionospheric RM (RM_{ion}; green triangles; right y-axis) and their uncertainties; the RM_{ISM} calculated from each RM_{obs}–RM_{ion}; and the electron density-weighted average magnetic field parallel to the LoS, calculated using Equation 1 and the DM and RM_{ISM}. The weighted means of the relevant measurements are shown by the grey dashed lines, and one standard deviation from the mean is shown by the grey shaded areas.

the RM_{ISM} values is –64.33 rad m^{-2} with standard deviation 0.06 rad m^{-2}. This RM_{ISM} value is in agreement with (<1.4× uncertainties), and approximately 7-times more precise than, the literature value from the pulsar catalogue: RM_{cat}=–63.7±0.4 rad m^{-2}. The catalogue value was measured using observations at several centre frequencies between 250–500 MHz, and taken over 40 years before the LOFAR observations (Manchester 1972). Manchester (1972) corrected the data for RM_{ion} using continuous records of the total ionospheric Faraday rotation obtained towards a geostationary satellite. We also calculated the weighted mean of the $\langle B_{\parallel} \rangle$ values, –2.961 μG, with standard deviation 0.003 μG. This is also in good agreement (within 1.3 times the uncertainties) with the value published in Manchester (1972). In addition, we found that the median RM dispersion for all of the FDFs to be σ_{RM}=0.0005 rad m^{-2}, which is Faraday thin. The RM dispersions for the whole pulsar set are further discussed in Section 3.1.

The mean uncertainties on the values for RM_{obs} and RM_{ion} are 0.01 and 0.08 rad m^{-2}, respectively. This is an example of the excellent precision of the measurements that can be obtained from using the low-frequency LOFAR data. This also indicates that the RM_{ISM} uncertainty is dominated by the current method for correcting RM_{ion}. The data in Figure 3, along with previous work, show that we can expect reasonably high accuracy in the measurement of RM_{ISM} us-

ing the current method for correcting for RM_{ion}, e.g., the standard deviation in the RM_{ISM} values for PSR B0329+54 is just 0.06 rad m^{-2}. However, it is clear that more sophisticated methods that are being developed for more accurately determining RM_{ion} will be essential towards fully realising the RM precision possible using low-frequency data (e.g. Malins et al. 2018), in particular for the LOFAR Low-Band Antenna observations. This will also allow us to fully realise higher $\langle B_{\parallel} \rangle$ precision, since the fractional uncertainties on the RM measurements are currently a factor of ≈100 larger than the fractional uncertainties on the DM measurements.

The results published in Table A1 include the RM_{obs} measured, the RM_{ion} estimates, and the resulting RM_{ISM} and uncertainties, along with the dates and times of the observations. This is to provide the possibility of applying more advanced ionospheric Faraday rotation corrections that may become available in the future.

3   RESULTS

Here, we summarise the results of the RMs determined towards pulsars using the LOFAR observations described.

We determined the RMs towards 117 pulsars in the non-recycled pulsar census and 19 pulsars in the MSP census (136 in total), presented in Table A1. This represents 74 and 40 per cent of all of the pulsars detected in each of the LOFAR censuses, respectively, and 86 and 60 per cent of the pulsars with total intensity S/N greater than 10, respectively. The pulsars in these censuses were not selected based on their polarisation characteristics (but on position accuracy, Galactic location, see Bilous et al. 2016; Kondratiev et al. 2016). Therefore, they form a reasonably representative sample of the proportion of pulsars that can be used to measure RMs below 200 MHz. The FDFs obtained towards each pulsar are shown in Appendix B.

The pulsars with RMs measured in this work are located between 14 and 321 degrees in Galactic longitude (although the majority are between 20–200 degrees) and –58 and 86 in Galactic latitude. The pulsar closest to the Galactic plane is PSR B1937+21, at Galactic latitude –0.29 degrees. The DM range is between 3 and 161 pc cm^{-3} (PSRs J1744–1134 and B2036+53, respectively). The RM_{ISM} range is between –168.7±0.1 and 154.9±0.2 rad m^{-2} (PSRs B2210+29 and B1848+13, respectively). The smallest absolute RM measurement, RM_{ISM}=0.96±0.09 rad m^{-2}, is towards PSR J0435+2749. The range in average magnetic field strength parallel to the LoS calculated is between –5.635±0.009 and 3.524±0.004 μG (for PSRs J2043+2740 and B1842+14, respectively). The uncertainties on these measurements provide examples of the accuracy that can be obtained for $\langle B_{\parallel} \rangle$, towards studying the Galactic magnetic field using the methods described.

Distance estimates for the pulsars (those without independent distance measurements) are calculated using the recently published Galactic electron density model from Yao et al. (2017), hereafter referred to as YMW16[11], this is further discussed in Section 4.5. The distance estimates for pulsars with RM measurements range from 0.2 to 25 kpc
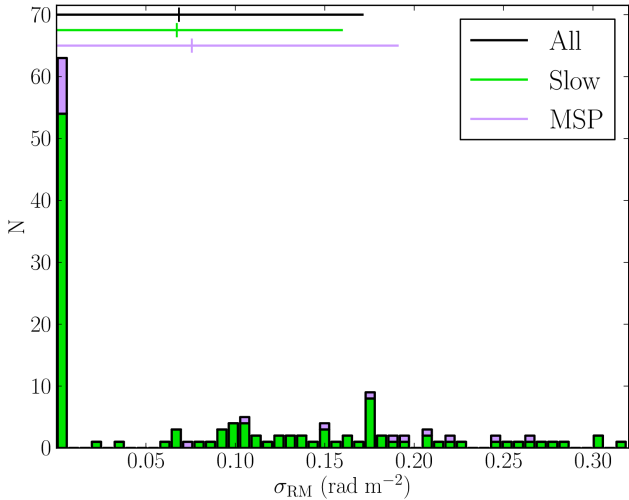
---

[11] www.xao.ac.cn/ymw16/

Figure 4. A stacked histogram showing the RM dispersion (σ_{RM}) for the pulsars in the 'slow' pulsar (green) and MSP (purple) censuses. The horizonal lines with corresponding colours above mark the range between the 25th and 75th percentiles, with the median shown by the vertical line (the complete pulsar set is shown by the black line).

(although the few pulsars with 25 kpc distances are likely overestimated, as this is the limit given by the model, see Section 4.5). The distances of the pulsars from the Galactic plane used in the analysis of the magnetic scale height of the Galactic halo is between –3 and 4 kpc, see Section 4.4.

3.1 RM dispersion results

Figure 4 summarises the RM dispersion, σ_{RM}, calculated by running RM CLEAN on the FDFs obtained towards each pulsar. The RM dispersion results for each pulsar are also included in Table A1. The RM dispersion bin with the largest number of pulsars (63) represents values less than 0.0009 rad m^{-2}. This is < 1 per cent of the typical RM uncertainty. Eight pulsars with S/N$_F$ >7 have RM dispersions that are indistinguishable from 0 rad m^{-2}, i.e., all of the components from RM CLEAN fall within the same pixel value after at least one RM CLEAN iteration. These are PSRs B0331+45, B0523+11, J0611+30, B0940+16, J1612+2008, J1645+1012, J1741+2758, and B2110+27. The median RM dispersion for the RMs in this work (from both censuses) is 0.068 rad m^{-2}, which is less than 10 per cent of $\delta\phi$, see Table 1. Furthermore, all of the values obtained are less than 40 per cent of $\delta\phi$. The RM dispersions of 75 per cent of the pulsars in this work are less than 0.17 rad m^{-2} and satisfy the Faraday thin criterion, $\lambda^2 \Delta\phi \ll 1$, even at the longest observing wavelength ($\lambda^2 = 7.4$ m^2). For the few pulsars that have larger RM dispersions, it is likely that this is largely due to RM CLEAN-ing too deeply in the presence of noise. All of the pulsars in this work satisfy $\lambda^2 \Delta\phi \ll 1$ at the shortest observing wavelength ($\lambda^2 = 2.5$ m^2). In addition, there is no evidence for emission at more than one RM value to a high degree of confidence, also as expected in FDFs obtained using pulsar data.

We investigated possible correlations between the RM dispersion and a number of parameters. We found no sig-

nificant correlation between the RM dispersion and: the number of bins used to extract the Stokes parameters from the pulse profiles; the S/N in the FDFs; the DMs; the absolute value of the measured RMs; or the uncertainty on the RMs. We also obtained published scattering measures, τ_{sc}, at 1 GHz from the pulsar catalogue for 54 of the slow pulsars and 3 of the MSPs (Manchester et al. 2005, and references therein) to investigate any correlation with the RM dispersion. Again, we found no significant correlation trend between these two variables. However, two pulsars with the largest scattering times also have among the largest RM dispersions measured. These are the Crab pulsar PSR B0531+21 with τ_{sc}=1.2×10^{-4} s at 1 GHz and σ_{RM}=0.25 rad m^{-2}; and PSR B1946+35 with τ_{sc}=4.1×10^{-4} s at 1 GHz and σ_{RM}=0.30 rad m^{-2}, see Section 4.3 for further discussion for the Crab pulsar. Whether some of the larger RM dispersions may in fact be the result of foreground diffuse ISM structures affecting the signal will require a more comprehensive study, using the calibrated polarisation profiles as a function of observing frequency.

The RM dispersions obtained using these LOFAR data show that the majority of the signals from the pulsars are extremely Faraday thin, as we expected. These low-frequency observations provide the most stringent information about the extent to which pulsars are Faraday thin, to date.

4 DISCUSSION

Here, we discuss the RM results that we obtained using the LOFAR observations and provide further analysis in combination with literature RM measurements. In Section 4.1 we examine the nature of the data for pulsars towards which we did not detect a significant RM. In Section 4.2 we compare the RMs that we measured at low-frequencies to measurements from the literature towards the same pulsars, as well as towards extragalactic sources along the same LoSs to provide further context. In Section 4.3 we briefly comment on the results for some individual pulsars. In Section 4.4 we further analyse the RMs towards pulsars to give estimates of the magnetic field scale height in the Galactic halo. In Section 4.5 we discuss the limitations of the data we currently have to study the Galactic magnetic field structure, and prospects for future improvements.

4.1 Detecting and measuring RMs

For the pulsars where we did not detect a significant RM with S/N$_F$ >4, the primary reason seems to be lower S/N in the pulse profile (resulting in lower S/N$_P$ in the pulse profile). The median S/N for the slow pulsars and MSPs that we did detect an RM for are 67 and 19, respectively. Meanwhile, the slow pulsars and MSPs that we did not detect an RM for have median S/N of 10 and 8, respectively. However, the lowest total intensity pulse profile S/N for which we did detect a significant RM is just 4 (for PSR J2002+1637), as this pulsar is highly polarised. For 14 pulsars (10 slow and 4 MSPs), we detected a tentative RM in the FDFs, but these were below the chosen S/N threshold set, S/N$_F$ >4, and so are not included in the final catalogue. Half of these pulsars do not have an RM published in the literature, and it is likely that a significant RM would be detected if a longer

integration time is used to increase the S/N in the average pulse profiles. Furthermore, the median DM of the pulsars with significant RMs is 35 pc cm^{-3}, while the median DM of the pulsars with no significant RM detection is almost double: 61 pc cm^{-3}. For the 'slow' pulsars, this is due to larger distances to the pulsars, which also reduces the flux density: the median distance estimates for pulsars with or without a significant RM detection are 2.2 kpc and 3.9 kpc, respectively. For the MSPs, this is not necessarily the case: the median distance estimates for MSPs with or without a significant RM detection are 1.2 kpc and 1.3 kpc, respectively. Therefore, is likely that dispersion smearing and/or scattering in some of the pulse profiles may also have an effect on the S/N and degree of polarisation of the signals, see below. The S/N$_P$ could be increased for pulsars that have been observed at least once (e.g. for timing/monitoring campaigns) by adding the datasets together (after correcting for ionospheric RM variations).

Several of the pulsars show evidence of scattering tails, in some extreme cases these increase to span almost the entire pulse phase (see Bilous et al. 2014; Geyer et al. 2017). Whether we can detect an RM in these data seems to vary on a case by case basis. In some cases where the pulsar is reasonably polarised at low frequencies we detected a significant RM, although more pulse phase bins may need to be summed (e.g. for PSR B1946+35 we summed 70 phase bins, or 7 per cent of the rotational period, to gain sufficient S/N). For others, the scattering may contribute to depolarising the signal towards low frequencies, e.g., PSR B2053+36 has RM$_{cat}$=−68.00 rad m^{-2}, but we were unable to detect a significant RM at our observing frequency. Furthermore, 29 of the pulsars towards which we did not detect a significant RM also do not have an RM published in the literature, listed in Table 2. It may be that the signal from some of these pulsars is intrinsically unpolarised, possibly due to the emission-beam–LoS geometry, orthogonal polarisation modes, or spin-down luminosity (e.g. Radhakrishnan & Cooke 1969; Manchester et al. 1975; Johnston & Kerr 2018).

For six pulsars, the peak in the FDF was within the range set for any expected instrumental polarisation ($-0.77 < \phi < 0.77$ rad m^{-2}) and since we cannot (using the current data processing methods) be confident whether the majority of the polarised signal is from the pulsar or the instrument, these results were not included in our catalogue. Most of these pulsars have small RM values (e.g. for PSR B1237+25 RM$_{cat}$=−0.12±0.06 rad m^{-2}) or have large fractional uncertainties (e.g. for PSR J1503+2111 RM$_{cat}$=−5±10 rad m^{-2}). Limits on the RMs for these pulsars could have been included by using the ionospheric RM calculated (mostly less than 1 rad m^{-2}). However, we can obtain more reliable measurements by re-observing these pulsars when the ionosphere is more ionised and imparts a more substantial RM$_{obs}$, e.g. during the day.

Six of the pulsars for which we did not detect a significant RM have absolute catalogued RMs larger than the expected maximum observable RM (i.e. ±163 rad m^{-2}, where ≈50 per cent sensitivity is lost due to bandwidth depolarisation, at the central observing frequency, see Table 1). The largest absolute RMs that we measured are approximately equal to this value: PSR J2017+2043 with RM$_{obs}$=−160.93 rad m^{-2} and PSR B2210+29 with RM$_{obs}$=−

Table 2. Summary of pulsars towards which we did not detect a significant RM in this work, and which also do not have an RM published in the literature.

PSR name	PSR name	PSR name	PSR name
'Slow' census	= 15		
J0006+1834	J1834+10	J1908+2351	J2040+1657
J0324+5239	J1848+0826	J1913+3732	J2048+2255
J0329+1654	J1900+30	J1937+2950	J2243+1518
J0711+0931	J1901+1306	B2025+21	
MSP census	= 14		
J0337+1715	J1544+4937	J1905+0400	J2215+5135
J1023+0038	J1709+2313	J1918-0642	J2302+4442
J1038+0032	J1738+0333	B1957+20	
J1231-1411	J1816+4510	J2019+2425	

165.23 rad m^{-2}. This is because the upper half of the bandwidth (149–188 MHz) can still be used to detect a significant signal (albeit with a slightly larger FWHM$_F$). For these pulsars, the RM measurement was verified and the S/N$_F$ increased by downloading higher frequency resolution data, available from the LOFAR Long-Term Archive (down to 30 kHz channel width). These data raise the maximum expected observable RM to ±1000 rad m^{-2} at the central observing frequency. The higher frequency resolution data was not used for all of the census pulsars because this is not necessary for pulsars with lower absolute RMs (this applies to the majority of the pulsars in the sample) and the data volume is over 6 times larger, increasing the download and processing times. We also downloaded the higher frequency resolution data and obtained FDFs for the six pulsars with larger catalogued RMs, but none resulted in a significant detection using the standard or higher frequency resolution data.

4.2   Comparison of results with literature measurements

We verified the RM results we obtained via a comparison with the RMs available in the literature (for 111 pulsars), see Figure 5. The comparison shows that there is very good agreement between the RM measurements. The line of best fit gradient is very close to the expected value of 1 (0.94±0.01; or 0.99±0.02 for an unweighted fit). Furthermore, the majority of measurements (for 102 pulsars) agree within 4 times the published uncertainties. This indicates that the RM uncertainties from the literature are likely generally underestimated. In the few cases with larger discrepancies, either the pulsar catalogue RM had no uncertainty reported (and listed as 0 rad m^{-2}), or both measurements have very small uncertainties and may have underestimated possible systematics due to, e.g., the ionospheric RM correction. This comparison of the RM measurements demonstrates that the RMs measured at low frequencies do not appear to show any disparity compared to those measured at higher frequencies. This confirms that there is no frequency-dependence in RM measurements and that the pulsar magnetosphere does not contribute to the observed RM, to the level of uncertainty to which we can currently measure, as we expected (e.g. Wang et al. 2011).

Furthermore, some independent RM measurements using LOFAR observations were published by Noutsos et al.
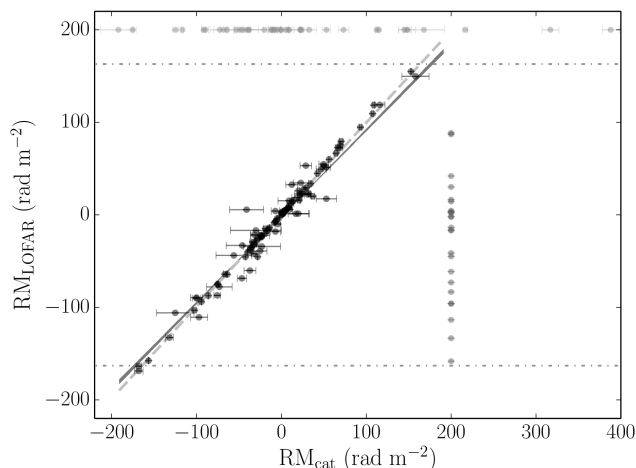
Figure 5. A comparison between the RMs obtained using LO-FAR in this work, RM_{LOFAR}, and the literature, RM_{cat}, (black points). The expected trend $RM_{cat}=RM_{LOFAR}$ is shown by the light grey dashed line. The line of best fit with uncertainties is shown by the dark grey line. The horizontal dash-dotted lines shows the $|\phi_{max}|$ at $|RM_{LOFAR}|$=163 rad m^{-2} for the centre frequency 149 MHz, see Table 1. The distribution of RMs obtained in this work without previous measurements are shown by the dark grey points at a constant RM_{cat}=200 rad m^{-2}. The distribution of RMs not detected in this work, but with literature measurements are shown by the light grey points at RM_{LOFAR}=200 rad m^{-2}.

(2015), 12 of which overlap with this work, see Table A2. Comparing the LOFAR RMs from Noutsos et al. (2015) and this work, the measurements generally agree within the uncertainties; there is a range in agreement from 0.02–2-times the uncertainties. This indicates that we derive reasonable uncertainties on the RMs by adding (in quadrature) the formal uncertainty on the RM measurement from the FDFs and the uncertainty on the RM_{ion} corrections.

The precision of the RM (and DM) measurements obtained using the low-frequency LOFAR data are illustrated in Figures 5 and 6. For the 111 pulsars with RMs in both the literature and in this work, the mean uncertainty from the pulsar catalogue and this work are 3.4 rad m^{-2} and 0.1 rad m^{-2}, respectively. The median fractional uncertainties on the RM measurements are 6.4 and 0.3 per cent, respectively. This indicates that the RMs measured using the low-frequency data are over 20-times more precise (on average) than literature measurements.

Currently, the most substantial contribution to the cumulative uncertainty on the low-frequency RM measurements is the ionospheric RM correction. The median uncertainty on the RM_{obs}, before ionospheric RM subtraction, is 0.02 rad m^{-2}. The median uncertainty for the RM_{ion} estimates is 0.08 rad m^{-2}. If future ionospheric corrections can be improved to the relative precision of the observed RM measurements, the uncertainties in the RM measurements can be improved by an order of magnitude. This will facilitate, for example, precise monitoring of RMs over time to measure and characterise small-scale magneto-ionic structures in the ISM.

Figure 6 shows the DM and modulus RM values towards the pulsars observed in this work, as well as from the pulsar catalogue, for DM < 250 pc cm^{-3} and |RM| < 204 rad m^{-2}.

Pulsars located towards low, medium, and high Galactic latitudes are identified using red, orange, and yellow colours, respectively. All of the pulsars with measured RMs from LO-FAR are shown, along with the pulsars with literature measurements (64 per cent of the pulsar catalogue within the DM and RM ranges). Also shown are stacked histograms for the DMs and modulus RMs for all of the pulsars in the scatter plots. The distributions approximate log-normal and power-law distributions, respectively. Pulsars towards higher Galactic latitudes tend to have lower DM and RM values, but are still distributed across a range in Galactic magnetic field strengths ($\lesssim \pm 4 \mu$G), similar to the mid and low ranges ($\lesssim \pm 6 \mu$G).

Figure 7 shows a summary of the current picture of the Faraday sky, along with fractional uncertainties. This includes the all-sky Galactic signal reconstructed from 41,632 RMs measured towards extragalactic sources (Oppermann et al. 2015); the 1133 RMs from the current pulsar catalogue (version 1.59; Manchester et al. 2005); and the 137 RM measurements (136 from the pulsar censuses, plus PSR B0329+54) obtained in this work. The large extragalactic catalogues provide densely-packed information about the LoS through the entire Milky Way across the majority of the sky (although measurements are more sparse in the southern sky), however mostly with larger fractional measurement uncertainties. Ongoing work with low-frequency surveys promises to reduce the fractional uncertainties in the extragalactic RM catalogue (e.g. Van Eck et al. 2018; Riseley et al. 2018). While future work using SKA pathfinder surveys promises to increase the number of extragalactic polarised sources further, e.g., MIGHTEE (MeerKAT International GHz Tiered Extragalactic Exploration Survey; Jarvis et al. 2016), POSSUM[12] (Polarisation Sky Survey of the Universe's Magnetism, using ASKAP), and VLASS[13] (VLA Sky Survey).

Complementary to the extragalactic information, the pulsar catalogue has fewer pulsars and, therefore, LoSs with RM measurements, the vast majority of which lie within a few degrees of the Galactic disc. However, the majority of these have much lower fractional uncertainties. Figure 7 also demonstrates the trend that (modulus) RMs decrease with increasing (absolute) Galactic latitude, also shown in Figure 6. A result of this is that the fractional uncertainties in the pulsar catalogue RMs (measured at higher observing frequencies) tend to increase with absolute Galactic latitude. The LOFAR measurements provide precise RM data towards pulsars located at a range of Galactic latitudes (above and below the plane, visible from the northern hemisphere) and show consistently low percentage uncertainties. This illustrates that the precision attainable using low-frequency observations is especially valuable for measurements where the absolute RM value is expected to be small, e.g., towards sources that are nearby or at larger absolute Galactic latitudes.

The median pulsar catalogue RM of the pulsars for which we did not detect a significant RM in the LOFAR data is 52.8 rad m^{-2}, with median absolute Galactic latitude and longitude 9.6 and 54.1 degrees, respectively. These pulsars

---

[12] http://www.dunlap.utoronto.ca/~askap.org/possum
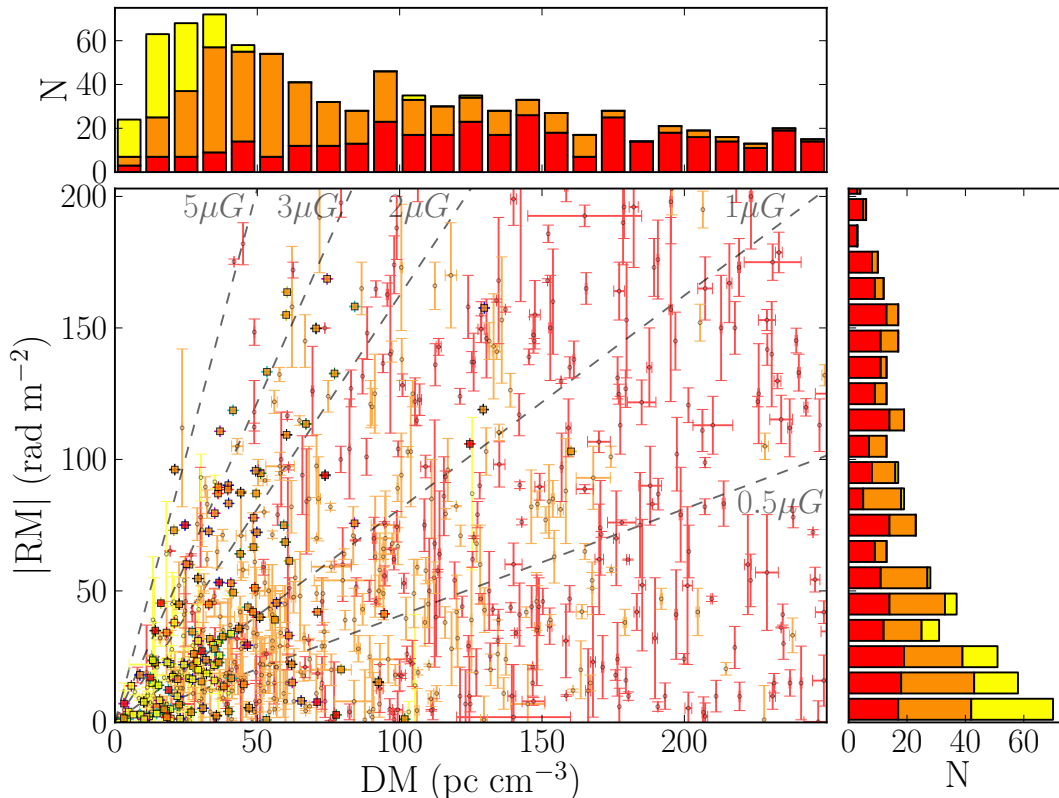[13] https://science.nrao.edu/science/surveys/vlass/vlass

Figure 6. Modulus RM values plotted against DMs for the pulsars with measurements from LOFAR (squares) and the pulsar catalogue (points). The colours represent pulsars at different Galactic latitudes (*b*) above and below the Galactic plane: |*b*| <5 degrees (red); 5⩽ |*b*| <30 degrees (orange); and |*b*| ⩾30 degrees (yellow). Lines of constant |⟨*B*∥⟩| are shown by the grey dashed lines and corresponding labels. The stacked histograms above/right show the corresponding distribution of all DM and |RM| measurements (with identical usage of colour).

are more likely to be in directions that tend to impart larger RMs, e.g., in the directions of the Galactic plane, the Galactic centre, the North Polar Spur and the boundary of Radio Loop I (large structures identified in the diffuse Galactic radio emission; e.g. Berkhuijsen et al. 1971; Dickinson 2018). Two pulsars in the pulsar census are located towards the plane and Radio Loop I and have catalogued RMs greater than the maximum observable RM attainable for the LOFAR data used (PSR J1859+1526, RM=317±10 rad m^{-2}; PSR J1906+1854, RM=388±10 rad m^{-2}). For comparison, the median absolute Galactic latitude and longitude of the pulsars that have a significant LOFAR RM are 14.9 and 94.2 degrees, respectively. Therefore, for pulsars in the direction of the Galactic plane and at more considerable distances, increasingly higher frequency observations are complementary to the lower frequency data to enable us to probe the Galactic volume in its entirety. Pulsars in these areas of the Galaxy will also be increasingly difficult to detect at low frequencies due to more substantial dispersion smearing and/or scattering due to the intervening thermal electrons in the ISM.

A reconstruction of the all-sky Galactic RM signal using extragalactic sources (from Oppermann et al. 2015), shown as the background in Figure 7, allows us to compare this information about the entire LoS through our Galaxy to the RMs towards pulsars (located at various distances from the

Sun). This indicates how much of the total Faraday depth along each LoS is probed by the foreground pulsars. If there are no large-scale magnetic field reversals in the Galactic halo, then we expect the RMs towards pulsars at greater distances to approach the RM values towards the extragalactic sources. Figure 8 shows the pulsar RMs (from the literature and this work; RM$_{PSR}$) compared to the same LoS directions from the all-sky Galactic RM map (RM$_{EGS}$) for all pulsar LoS located towards Galactic latitudes |*b*| > 5 degrees (473 points), coloured according to the pulsar's distance estimates. Although the points seem to be somewhat scattered, 77 per cent of the RM$_{PSR}$ and RM$_{EGS}$ have the same sign. Making cuts for pulsars at lower Galactic latitudes (e.g. |*b*| > 2 degrees) reduces this proportion (74 per cent), since closer to the plane there are more likely to be large-scale field reversals and small-scale structures associated with turbulence in the ISM. Making cuts for pulsars at greater Galactic latitudes (e.g. |*b*| > 8 degrees) increases this proportion (79 per cent).

We further divided the points in Figure 8 into three distance bins based on the pulsar distance estimates: 'close', 'medium', and 'distant', divided by the 33rd and 66th percentiles of the distances (d⩽1.5 kpc, 1.5<d⩽3.5 kpc, and d>3.5 kpc, respectively). The correlation coefficient (r-value) between RM$_{PSR}$ and RM$_{EGS}$ is positive for all distance bins. When reducing the sample to all RMs with the same signs,
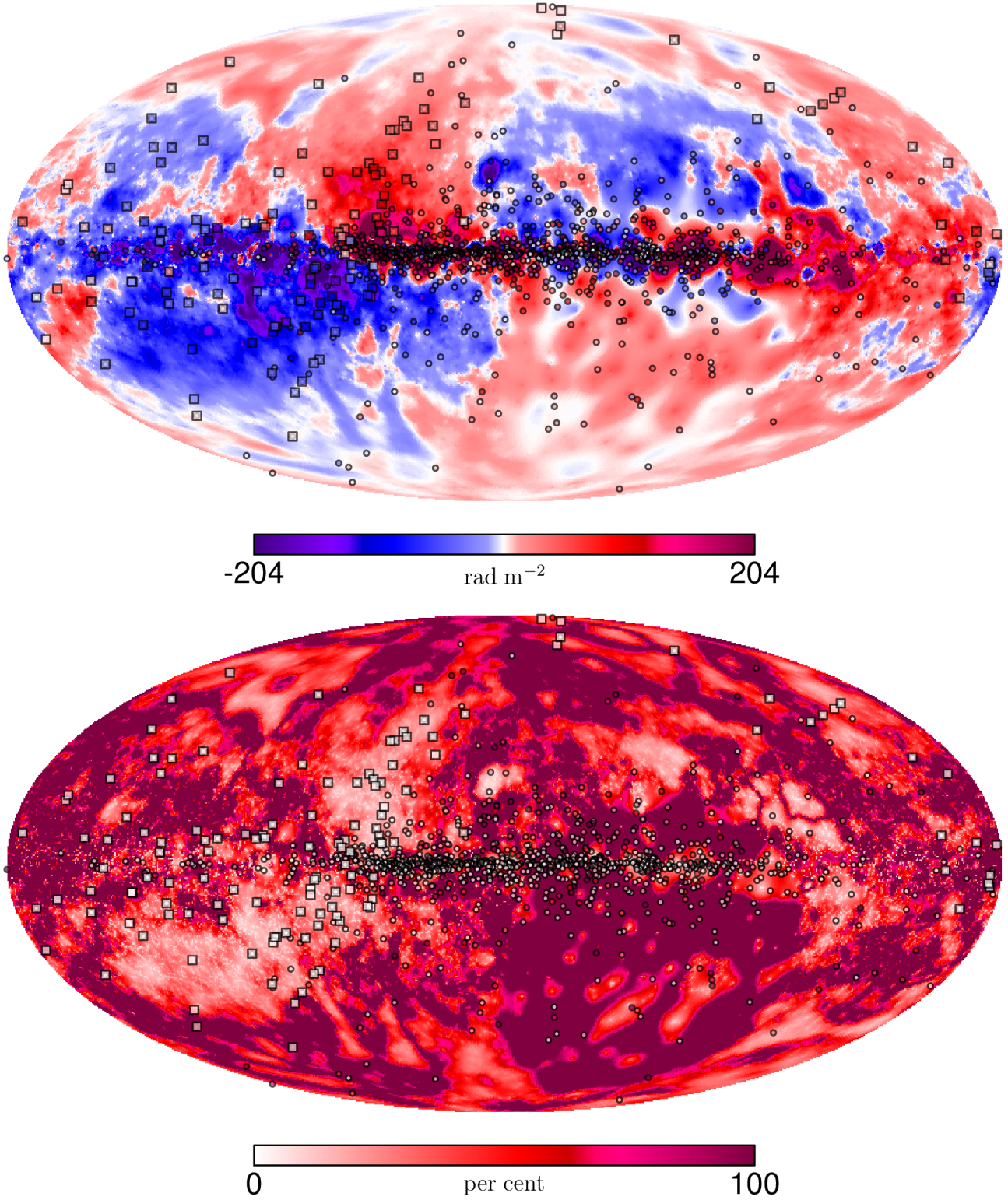
Figure 7. Upper: The RM sky shown in Galactic coordinates using Mollweide projection with $\ell, b = 0$ degrees at the centre. The background shows the all-sky Galactic RM signal reconstructed using extragalactic sources. The points show the 1133 RMs from the pulsar catalogue. The squares show the 137 RMs from this work using LOFAR. All data are plotted using the same colour scale, shown by the colour bar in rad m^{-2}, saturated at a cut-off of ±204 rad m^{-2} to emphasise the RM range of the LOFAR data. Positive RMs (reds–pinks) show where the net GMF direction is towards the Earth, and negative RMs (blues–purples) show where the net GMF direction is away from the Earth. Lower: Percentage uncertainties corresponding to the measurements in the upper plot, with corresponding markers. All uncertainties are shown using the same colour scale, shown by the colour bar in per cent and truncated at 100 per cent measurement uncertainty.

Figure 8. A comparison between the RM towards the pulsars located at $|b| > 5$ degrees, RM_{PSR}, and the Galactic RM signal reconstructed using extragalactic sources, RM_{EGS}, towards the corresponding LoSs. The points are coloured according to each pulsars' distance estimate in parsecs, shown by the colour bar.

the correlation coefficients are: 0.76, 0.85, and 0.78, respectively. Again, making cuts for pulsars at lower latitudes (e.g. $|b| \geqslant 3$ deg), the r-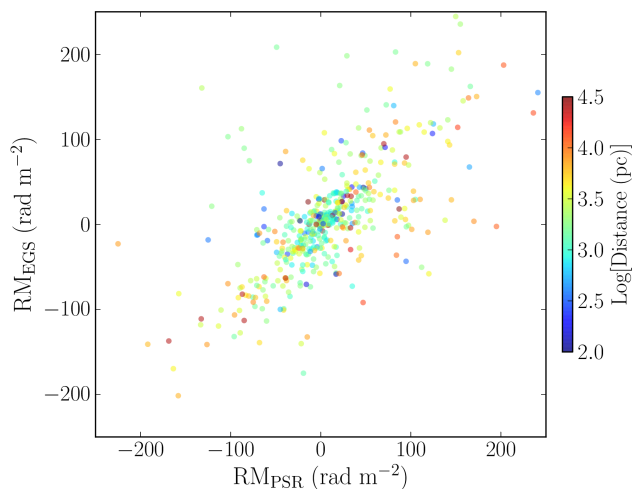values decrease, except for the pulsars in the 'distant' bin. Making cuts for pulsars at greater latitudes (e.g. $|b| \geqslant 10$ deg), the r-values increase in all bins and are 0.9 for the 'medium', and 'distant' bins. This indicates that RM_{PSR} and RM_{EGS} tend to become more correlated for pulsars at greater distances, as expected if there are no large-scale field reversals in the Galactic halo magnetic field. However, the variables are perhaps not as well correlated as expected. This may be because at more considerable distances, the distance estimates towards pulsars become more uncertain, see Section 4.5 for further discussion. The differences in the correlation coefficients for different cuts in $|b|$ also indicates that the RMs towards pulsars may have varying contributions from small-scale magneto-ionic foreground structures, for example, supernova remnants or HII regions (e.g. Mitra et al. 2003), which are usually more numerous closer to the Galactic plane compared to higher latitudes, also discussed in Section 4.3. This highlights the requirement for collecting a large set of pulsar RMs for the purpose of studying the large-scale GMF, so that the contributions from small-scale ISM structures may be identified and down-weighted or averaged out in reconstructions of the large-scale GMF structure.

4.3   Notes on individual pulsars

The RM measurements towards the Crab Pulsar B0531+21 (located within the Crab Nebula supernova remnant) show a discrepancy of 5.4-times the uncertainties: the pulsar catalogue value measured over 40 years ago is $RM_{cat}=-42.3 \pm 0.5$ rad m^{-2} (Manchester 1972) and the RM value measured in this work is -45.44 ± 0.08 rad m^{-2}. It is possible that the difference in RM may be because of variations between the observing epochs. Unfortunately, there are very few published RM measurements towards the Crab pulsar for epochs besides these. However, there are monthly updates for other

Crab ephemeris parameters[14], including for the DM (Lyne et al. 1993). Between 1988 May to 2018 September, the minimum and maximum DMs measured were 56.734 pc cm^{-3} and 56.921 pc cm^{-3}, respectively. The median DM measured during this time period is 56.7805 pc cm^{-3}, which is closer to the value from the LOFAR measurement on 2014 February 15 of 56.7712 pc cm^{-3}. Assuming that the magnetic field value $\langle B_{\parallel} \rangle$ stays constant, see Table A1, the maximum DM measured would increase the RM by 0.12 rad m^{-2}. This does not account for the 3.1 rad m^{-2} difference between the RM measurements, indicating that the magnetic field value may also vary along with the electron density.

Such a variation in RM with time has also been observed for the Vela Pulsar B0833–45, located in the Vela Supernova Remnant (e.g. Johnston et al. 2005; Lenc et al. 2017). In these cases, there seem to be small fractional changes in the RMs, with no change in the sign of the RM. Therefore, it is likely that we are sensing both the coherent large-scale Galactic magnetic field component, plus some contribution from a random small-scale foreground magnetic field component, e.g., within the associated supernova remnant structure. In addition, the RM dispersion measured towards the Crab Pulsar, $\sigma_{RM} < 0.25$ rad m^{-2}, is above the 92nd percentile of σ_{RM} measurements in this work. This may also suggest some random variations in the magnetic field along the LoS probed by different propagation paths due to scattering, but again, this can be further investigated in more detail using the polarisation profiles in future work. Repetition of observations to monitor these RM variations over long, ~years, timescales could allow us to estimate the strength and variance of the random magnetic field components associated with the small-scale foreground structure, and deduce the ratio between this and the large-scale, coherent component.

PSR J1810+1744 is an eclipsing black widow pulsar (it is in a short orbital period binary system with a low-mass companion star; e.g., Breton et al. 2013). The RM towards this source has not been published in the literature. In this work, we measured the RM, 88.5 ± 0.1 rad m^{-2}, using a 20-minute observation with a total intensity S/N of 6, see Table A1. Shorter integration times further reduce the S/N, making investigating changes in RM on short timescales over the binary period difficult, as has previously been studied for DM and scattering parameters (Polzin et al. 2018). For the single-epoch observation used in this work, the RM dispersion measured shows that the source is Faraday thin: <0.0004 rad m^{-2}.

Another black widow pulsar that was observed as part of the LOFAR MSP census is PSR J2051–0827. This pulsar is also subject to repeated timing observations using LOFAR, providing data for multiple different phases of the binary period. The polarisation profile and RM results will be presented in future work (Polzin et al., in prep.).

Some of the pulsars observed in this work are known to change emission modes, e.g. PSR B0823+26 (Sobey et al. 2015; Hermsen et al. 2018), and PSR B0943+10 (Hermsen et al. 2013; Bilous et al. 2014). These pulsars were in the 'bright' emission mode during the observations used to measure the RMs for this work. PSRs B0823+26 and B0943+10

---

[14] http://www.jb.man.ac.uk/pulsar/crab.html

are among the timing set that are repeatedly observed by LOFAR, and a possible correlation between RM and intrinsic emission mode (although not necessarily expected) will be explored in future work.

4.4 Scale height of the Galactic halo magnetic field

Although there are fewer RM measurements towards pulsars compared to the extragalactic catalogue (e.g. Oppermann et al. 2015), the additional DM information provided by pulsars allows us to infer the electron-density-weighted average magnetic field parallel towards each LoS. The pulsars are distributed throughout the Galaxy at a range of heights (Z) above/below the Galactic disc, obtained using the YMW16 Galactic electron density model. To demonstrate this, Figure 9 shows the locations of the pulsars in the Galaxy on a 3-D plot in cartesian coordinates. The Sun is located at (X,Y,Z)=(0,8.3,0.006) kpc and the Galactic Centre is at (X,Y,Z)=(0,0,0) kpc, as in YMW16, and the Galactic quadrants are also labelled. The markers in Figure 9 are coloured according to the inferred magnetic field strength $\langle B_\parallel \rangle$ and direction. The X–Z and Y–Z slices are also shown for further clarity. Figure 9 demonstrates that these data can provide a measurement of the scale height of the Galactic magnetic field in the halo.

Figure 10 shows the magnetic field parallel to the LoS, $\langle B_\parallel \rangle$, calculated for the pulsars in this work, as well as those from the literature, as a function of their vertical distance from the Galactic plane, Z. All pulsars located in Galactic quadrant I between galactic longitude $30 \leqslant \ell \leqslant 90$ degrees are shown as orange points, and all pulsars located in Galactic quadrant II between galactic longitude $90 \leqslant \ell \leqslant 180$ degrees are shown by the violet points. These ranges were chosen to investigate the directions towards the inner Galaxy (excluding regions closer towards the Galactic centre) and the outer Galaxy, respectively. These are also the ranges where the largest number of pulsars with LOFAR data are located, see Figure 9.

Figure 10 shows that for Galactic quadrant I, there is a notable dichotomy between mostly positive (negative) magnetic field values for pulsars located above (below) the plane, similarly evident in Figure 7. Although the large region of positive $\langle B_\parallel \rangle$ seems to be coincident with the North Polar Spur feature (e.g. Sun et al. 2015), this effect may be somewhat related to the large-scale magnetic field reversal in the Galactic plane in this quadrant (e.g. Van Eck et al. 2011). However, the large-scale reversal does not appear to affect the bulk sign of the RM either above or below the Galactic plane and perhaps the effect of the large-scale reversal may not be visible in the halo and confined to the plane. Conversely, in Galactic quadrant II, where a large-scale magnetic field reversal is not expected (e.g. Van Eck et al. 2011), there is a majority of negative magnetic field values towards pulsars located both above and below the plane. Although the pulsar data are more sparse towards the Galactic anticentre, with half of the number of data points compared to quadrant I and 35 per cent more data points below the plane. For comparison, in quadrant I there are approximately equal numbers of points above and below the plane. The median magnetic field strengths and directions in Galactic quadrants I and II using these data are 0.76 and
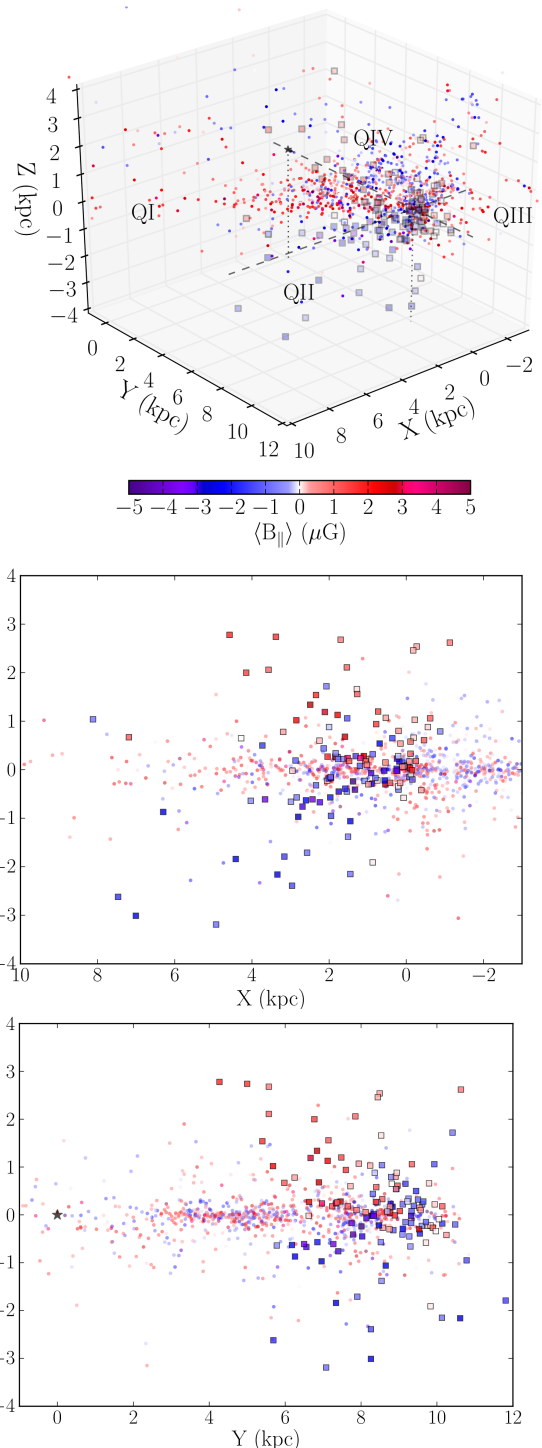
Figure 9. Upper: 3-D plot showing the location of pulsars, in Galactocentric coordinates, with colours representing $\langle B_\parallel \rangle$ in µG, see colour bar. The points show the pulsars with DM and RM measurements from the literature. The squares show the pulsars with DM and RM measurements from this work using LOFAR. The location of the Galactic Centre is shown by the black star, with the black dotted line connecting it to the x-y axis. The Galactic quadrants are labelled QI–IV, and separated by the dashed lines. The intersection of the lines show the location of the Sun, which is also connected to the x-y plane by the grey dotted line. Middle, Lower: The same points from the upper plot are shown in the X-Z, and Y-Z planes, respectively. 18 pulsars (10 with literature RMs and 8 with LOFAR RMs) have larger Z values (>8 kpc) and are not shown here.
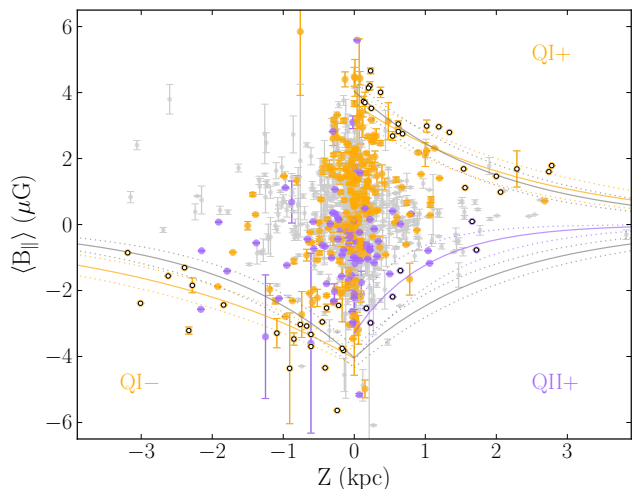
Figure 10. Using the RM and DM measurements from the pulsar catalogue and this work, $\langle B_\parallel \rangle$ is shown against the estimated height above/below the Galactic plane, Z, (grey points). The pulsars located in Galactic quadrant I in the range $30 \leqslant \ell < 90$ degrees are shown by the orange points, and pulsars located in Galactic quadrant II in the range $90 < \ell < 180$ degrees are shown using the violet points. Three areas in the plot are identified: Galactic quadrant I, above the plane, with positive $\langle B_\parallel \rangle$ values (labelled QI+ in orange); Galactic quadrant I, below the plane, with negative $\langle B_\parallel \rangle$ values (labelled QI– in orange); and Galactic quadrant II, above the plane, with negative $\langle B_\parallel \rangle$ values (labelled QII+ in violet). The 'outermost' points identified (see text) in these areas are shown by the open circles. Fits of the magnetic scale height to the 'outermost' points using Equation 5 (solid lines) and the uncertainties (dotted lines) are shown for QI+ and QI– (orange lines) and QII+ (violet lines). We also show the fit for the magnetic scale height to all of the absolute values of the outermost points (grey solid line) and the uncertainties (grey dotted lines) for comparison.

–0.77 µG, respectively. These values are consistent with the strength of the regular halo magnetic field of 2 µG or lower from Sun & Reich (2010).

We use the data shown in Figure 10 to fit for the magnetic scale height in the Galactic halo, using the form:

$$\langle B_\parallel \rangle = \langle B_{\parallel,0} \rangle \exp(-Z/H), \tag{5}$$

where $\langle B_{\parallel,0} \rangle$ is the largest value of the magnetic field at Z=0, and H is the magnetic scale height. Both $\langle B_\parallel \rangle$ and Z can take positive and negative values depending on the areas identified in Figure 10. Since the RM data provide the magnetic field strength and net direction parallel to the LoS, these will provide a lower limit for the scale height of the total GMF. Therefore, we fit the 'outermost' points for pulsars in: Galactic quadrant I above the plane where $\langle B_\parallel \rangle > 0$ (labelled QI+); Galactic quadrant I below the plane where $\langle B_\parallel \rangle < 0$ (labelled QI–); and in Galactic quadrant II above the plane where $\langle B_\parallel \rangle < 0$ (labelled QII+), see Figure 10. The 'outermost' points were identified as the largest absolute values of $\langle B_\parallel \rangle$ in the bin ranges $0.1 < |Z| \leqslant 0.5$ kpc, $0.5 < |Z| \leqslant 1.5$ kpc, and $1.5 < |Z| \leqslant 3.5$ kpc. For the areas QI+ and QI–, the number of points selected in each Z bin was chosen to be one fewer than the total number of data points in the bin with the fewest number, i.e., in the bin $1.5 < |Z| \leqslant 3.5$ kpc. For the area QII+ with fewer data points, the number of

Table 3. Summary of the parameters obtained from fitting the magnetic scale height function in Equation 5. Uncertainties (±) are quoted in the columns to the right of the values.

Quadrant	Magnetic scale height (H)	±	$\langle B_{\parallel,0} \rangle$	±
	kpc	kpc	µG	µG
QI+	2.4	0.4	3.7	0.4
QI–	3.3	0.6	4.0	0.2
QII+	1.0	0.3	3.3	0.8
All	2.0	0.3	4.0	0.3

points in the $1.5 < |Z| \leqslant 3.5$ kpc bin is 2, and so 2 points were also selected from the $0.1 < |Z| \leqslant 0.5$ kpc and $0.5 < |Z| \leqslant 1.5$ kpc bins. Pulsars in Galactic quadrant II below the plane where $\langle B_\parallel \rangle < 0$ were not fit as there are insufficient data. The 'outermost' data points fit in each area are shown as open circles in Figure 10. Table 3 summarises the parameters obtained from the magnetic scale height fit using Equation 5. We also fit the scale height for the absolute values of all of the points fit in the individual areas, shown by the grey lines in Figure 10 and included in Table 3.

Table 3 shows that the general magnetic scale height found using the data for all areas identified in Figure 10 is 2.0±0.3 kpc. The mean of the magnetic scale heights for the identified areas is 2.2±0.5 kpc. All of the scale heights presented in Table 3 agree within the uncertainties, except for the QII+ area. This indicates that the scale height in Galactic quadrant I towards the inner Galaxy is larger than the scale height in Galactic quadrant II towards the outer Galaxy. Only six data points were fit for the QII+ area, and so a larger sample would be necessary to provide a more confident outcome for the direction of the outer Galaxy. All of the $\langle B_{\parallel,0} \rangle$ values in Table 3 agree within the uncertainties, and the value for all areas is 4 µG. We extrapolated the electron-density-weighted average magnetic field to a greater distance from the galactic plane (±6 kpc) using the results summarised in Table 3. At this height, the $\langle B_{\parallel,0} \rangle$ in areas QI+, QI–, QII+, and 'All' are 0.3±0.1 µG, −0.6±0.2 µG, −0.01±0.02 µG, and 0.2±0.1 µG, respectively.

The uncertainties from the fits are shown in Figure 10 and Table 3, and account for the uncertainties in the measurement of $\langle B_\parallel \rangle$, but not in Z, which are generally not known for pulsars with distance estimates but may have larger fractional uncertainties than the uncertainties on $\langle B_\parallel \rangle$. There are 5 and 3 data points in QI+ and QI–, respectively, that were not included in the fits because their |Z| distance estimates are much larger than the general population (> 8 kpc) and likely overestimated. The small uncertainties on $\langle B_\parallel \rangle$ from the LOFAR data at high |Z| values tend to flatten the fits (especially in QI–), increasing the scale height and decreasing the $\langle B_{\parallel,0} \rangle$ output. Therefore, higher numbers of pulsar data points with smaller uncertainties, especially at high |Z| values, are desirable for increasing the accuracy of determining the magnetic scale height(s) in future. Also valuable towards this goal are independent distance estimates for these pulsars, see Section 4.5 for further discussion.

The magnetic scale height summarised in Table 3 is comparable, although generally somewhat larger than, the Galactic free electron vertical scale heights determined using pulsar DMs, e.g. $1.8^{+0.1}_{-0.3}$ kpc from Gaensler et al. (2008); $1.4^{+0.3}_{-0.2}$ kpc from Savage & Wakker (2009); 1.6±0.3 kpc from

Schnitzeler (2012); or 1.67±0.05 kpc from YMW16. This corresponds to the thick disc of the Galaxy, which has a more extensive scale height than the thin disk with scale heights between 20–70 pc (e.g. Yao et al. 2017, and references therein). Since the Faraday rotation effect is caused by both the electron density and the magnetic field in the ISM, the scale heights obtained using RMs will not be independent of the electron density scale height. This may be why the scale height found here is also larger than the 0.74 kpc exponential scale height of synchrotron emission found in, e.g., Sun & Reich (2012). Although, in this case, synchrotron modelling also requires ancillary parameters, such as the relativistic electron population, and is also sensitive to the magnetic field perpendicular to the LoS. This provides an incentive to use at least one magnetic field observable to derive the properties and structure of the total GMF, including the anisotropy of the Galactic halo magnetic field, see Section 4.5. There are complex analytical models for large-scale Galactic halo magnetic fields (e.g. Ferrière & Terral 2014). Which of these models best fit the RM data will be explored in future work.

The scale heights determined for the Milky Way can also be compared to external galaxies. For example, for the edge-on galaxies NGC891 and NGC4631, Hummel et al. (1991) deduced scale heights of 0.9 kpc and 1.3 kpc, respectively, using the increase in the mean degree of polarisation with distance from the galactic disk. The numbers obtained here are also comparable or up to three times larger than these edge-on galaxies. The scale heights estimated here are also approximately equivalent to or greater than the radio scale heights seen in other galaxies (e.g. Krause et al. 2018).

4.5 Limitations of current data and future prospects

In future, polarisation calibration will be performed on the data described in this work, to present the low-frequency polarisation profiles. This may increase the S/N in linear polarisation for some pulsars so that an RM may be detected. In the cases where the linearly polarised S/N was less than the threshold set (i.e. S/N$_F$ < 4), it would be preferable to observe these sources for longer integration times to obtain more reliable detections and decrease the uncertainties. For pulsars that are being repeatedly observed in LOFAR timing campaigns (this includes a subset of both MSPs and 'slow' pulsars) the S/N in the polarisation profiles can also be increased by concatenating observations. However, ionospheric RM corrections will have to be made before the addition in this case. For this set of pulsars with higher S/N detections, the repeated observations can also be used to better constrain the RM (and uncertainty) after correcting for the ionospheric RM for several independent epochs, as was done as an example in this work for PSR B0329+54. The precise measurements now routinely obtained using low-frequency observations ushers us into an era where ISM parameters such as DMs, RMs, and scattering (e.g. Geyer et al. 2017; Michilli et al. 2018a) can be monitored over time, also allowing us to probe small-scale turbulent structures in the ISM and other foregrounds (e.g. Howard et al. 2016; Tiburzi & Verbiest 2018).

The maximum absolute RM measured in this work is towards PSR B2210+29 (RM$_{obs}$=−165.23 rad m^{-2}; RM$_{ISM}$=−

168.66 rad m^{-2}, after the ionospheric correction). Due to the channel widths used for the data set, the largest Faraday depth to which one loses 50 per cent sensitivity, at the centre frequency, is 163 rad m^{-2} (not accounting for the loss of frequency information due, e.g., to excised RFI). It is possible to use smaller channel widths for LOFAR observations, expanding this largest Faraday depth beyond 1000 rad m^{-2}. These data were not used in this work, as the data volume becomes more substantial and the data reduction more cumbersome. However, for areas where larger RMs are expected (e.g. towards the Galactic plane, at larger distances, and towards the boundary of Radio Loop I), also usually accompanied by larger DMs, the finer channel resolution can be utilised to detect the pulsars and measure larger absolute RMs. Probing the Galaxy in the Galactic plane and at more considerable distances, DMs and RMs measured using higher frequency observations will be complementary to the measurements from low-frequency observations. This is because pulsars with large DMs and RMs may become scattered or depolarised in lower-frequency observations. In this work, we demonstrated that the low-frequency LOFAR observations provide excellent fractional uncertainties on RMs (and DMs) towards pulsars with relatively low absolute RMs, e.g., that are located towards the Galactic halo and are relatively close to the Sun.

More pulsars are being discovered in ongoing pulsar surveys at various centre frequencies, including at low radio frequencies using LOFAR (e.g. Coenen et al. 2014; Michilli et al. 2018b; Tan et al. 2018). The pulsars discovered can be followed up with polarisation observations to obtain RM measurements, to increase the numbers of LoSs with which we can probe the structure of the Galaxy. The low-frequency discoveries are valuable because they are located relatively nearby or towards the Galactic halo (e.g. van Leeuwen & Stappers 2010). This provides local GMF estimates, which can be compared to the data from more distant pulsars or extragalactic sources for longer path lengths through the Galaxy. Moreover, pulsars at larger distances and in the Galactic plane are preferentially discovered at higher frequencies using other large radio telescopes (e.g. Stovall et al. 2014; Ng et al. 2014; Lyne et al. 2017), and are useful for mapping the GMF towards the more distant areas of our Galaxy. More known pulsars that are distributed throughout the Galaxy at various distances from the Sun provide more data with which to reconstruct the GMF structure (including any field reversals along the LoSs) with greater confidence. In the future, the observational capabilities of the SKA to discover and time pulsars will allow us to approximately triple the number of known pulsars in the Galaxy (e.g. Keane et al. 2015; Xue et al. 2017), as well as measure their parallax and proper motions using VLBI (e.g. Paragi et al. 2015), enabling 3-D tomography of the electron density and GMF (e.g. Han et al. 2015).

In order to reconstruct an accurate model of the GMF (and electron density) using RMs and DMs towards pulsars, it is becoming increasingly necessary to determine independent distance measurements towards larger numbers of pulsars. For the set of pulsars with RMs measured in this work, 17 slow pulsars and 13 MSPs (15 and 68 per cent of the set, respectively) have one (or more) independent distance measurements (see Yao et al. 2017, and references therein): via annual parallax using VLBI (14 slow and 5 MSPs, respec-

tively), or timing (0 and 6, respectively); association with a nebula (1 and 0, respectively); kinematic distances from HI absorption measurements (2 and 0, respectively); or an optical counterpart association (0 and 2, respectively) (Jennings et al. 2018). Although pulsar distances can be estimated using a Galactic electron density model, and these are becoming more accurate with more independent distance measurements that can be used to calibrate the models, there are still large numbers of pulsars for which distances are over 40 per cent uncertain (Yao et al. 2017). We used the recently published YMW16 electron density model for this work because previous models had a maximum |Z| limit of ⩽2 kpc. The YMW16 model allows larger heights above the Galactic plane, e.g. shown in Figure 10, facilitating the magnetic scale height fit. There are efforts towards increasing the number of pulsars with independent distance measurements, e.g., Deller et al. (2018) provide an annual parallax for a further 21 pulsars with RMs in this work. For these pulsars, the median discrepancy between the DM distance estimates and the VLBI annual parallax distance measurements is 0.67 kpc (or 54 per cent fractional difference). However, in a couple of extreme cases, the DM distance estimates are overestimated by ≈20 kpc for PSRs B2303+30 and B2210+29 towards Galactic coordinates $\ell \approx 90$, $b \approx -25$. It is essential to continue to obtain independent distance measurements for more pulsars so that 3-D tomography of the Galactic (magnetic field) structure using the precise ISM parameters measured using the SKA and its precursors can be fully realised (e.g. Han et al. 2015).

Studies using RMs alone cannot distinguish between ordered random and isotropic random field components, which are often grouped into the 'random' field component (e.g. Jaffe et al. 2010). Moreover, Equation 1 assumes that the magnetic field and thermal electron density are uncorrelated. However, if their fluctuations are (anti)correlated, this will yield an (under)overestimate of $\langle B_\parallel \rangle$, and can result in error by a factor of 2–3 in a statistically homogeneous magneto-ionic medium (Beck et al. 2003). Therefore, combining results from the other magnetic field tracers is desirable, to obtain as complete a picture of the 3-D GMF structure as possible. In the near future it may also be possible to include observations of the directions of arrival of Ultra-High Energy Cosmic Rays, but the sources and composition of these still need to be constrained (e.g. Aab et al. 2018, and references therein). The framework required to combine multiple observables, as well as theoretical models, to infer the most likely model of the structure of the Galaxy is being constructed and refined (e.g. IMAGINE; Boulanger et al. 2018). In the future, the SKA will also provide groundbreaking observations for many of the complementary observables of the GMF, particularly with respect to diffuse polarisation, extragalactic RM-grids, and Zeeman splitting (Haverkorn et al. 2015; Johnston-Hollitt et al. 2015; Robishaw et al. 2015, respectively), promising to revolutionise our understanding of the GMF.

5 CONCLUSIONS

(i) We have measured RMs towards 137 pulsars using the 'LOFAR census of non-recycled pulsars' (Bilous et al. 2016), the 'LOFAR census of millisecond pulsars' (Kondratiev et al.

2016), and repeated timing/monitoring observations of PSR B0329+54. We present the largest low-frequency RM catalogue to date, with 25 pulsars that do not have RMs published in the literature. For the remaining pulsars with previously published measurements, the low-frequency data generally agree with previous measurements, within uncertainties, and provide 20-times greater precision, on average. The RMs were corrected for ionospheric Faraday rotation using the IONFR code, with IGS VTEC maps and the IGRF-12 as inputs. This correction is essential for low-frequency data, where the largest contribution to the uncertainty is the current method for subtracting the ionospheric RM.

(ii) The RMs were measured using the RM-synthesis method and the RM dispersion, σ_{RM}, was obtained using the RMCLEAN algorithm. The RM dispersions show that the majority of the pulsars are Faraday thin sources: <0.001 rad m^{-2}. However, in some cases, e.g., the Crab Pulsar B0531+21, the larger RM dispersion found may be due to small-scale magneto-ionic structure associated with its supernova remnant.

(iii) We used the current RM and DM measurements available from the pulsar catalogue and this work to measure the magnetic scale height of the GMF in the halo, for a range of Galactic longitudes towards Galactic quadrants I and II, where the majority of the LOFAR measurements are located. Fitting all points, we found a general scale height of 2.0 ± 0.3 kpc – comparable to the scale height of Galactic free electrons published in the literature. Although distance estimates are available for all pulsars, independent distance measurements, e.g., annual parallax measurements, are important for the purpose of reconstructing the magnetic scale height in the halo and the GMF structure in general.

(iv) The RM measurements from this work present an initial precise catalogue, which will be expanded and also increased in accuracy by using the LOFAR timing data towards a set of slow pulsars and MSPs. Precise DMs and RMs from low-frequency instruments, such as these from LOFAR, are becoming routine, promising an era of monitoring for time variability, which can be used to further investigate, for example, small-scale foreground ISM structures.

(v) The results from the low-frequency pathfinder/precursor telescopes show the promise of the SKA. For example, the low-frequency SKA precursor in the southern hemisphere, the MWA, is also routinely observing pulsars (e.g. Xue et al. 2017). The DM and RM measurements the MWA can provide are complementary to LOFAR, from which an all-sky low-frequency catalogue can be assembled, allowing us to study the 3-D Galactic magnetic field structure in more detail. In the future, the SKA will revolutionise our knowledge of pulsars, magnetism, and our Galaxy through discovering, timing, and measuring the astrometric properties of a large number of pulsars in our Galaxy. Efforts towards an RM-grid of extragalactic sources, diffuse Galactic synchrotron emission maps and Zeeman splitting will also supply complementary magnetic field observables to reconstruct a more complete picture of the total GMF structure. Bayesian inference frameworks such as IMAGINE can enable us to combine these observables and theoretical models and to assess the likely (magnetic) structure of our Galaxy.

ACKNOWLEDGEMENTS

REFERENCES

Aab A., et al., 2018, ApJ, 853, L29

Aharonian F., Bykov A., Parizot E., Ptuskin V., Watson A., 2012, Space Sci. Rev., 166, 97

Anderson C. S., Gaensler B. M., Feain I. J., Franzen T. M. O., 2015, ApJ, 815, 49

Beck R., 2001, Space Sci. Rev., 99, 243

Beck R., 2009, in Strassmeier K. G., Kosovichev A. G., Beckman J. E., eds, IAU Symposium Vol. 259, Cosmic Magnetic Fields: From Planets, to Stars and Galaxies. pp 3–14 (arXiv:0812.4925), doi:10.1017/S1743921309030014

Beck R., Shukurov A., Sokoloff D., Wielebinski R., 2003, A&A, 411, 99

Beck R., et al., 2015, Advancing Astrophysics with the Square Kilometre Array (AASKA14), p. 94

Beck M. C., Beck A. M., Beck R., Dolag K., Strong A. W., Nielaba P., 2016, J. Cosmology Astropart. Phys., 5, 056

Berkhuijsen E. M., Haslam C. G. T., Salter C. J., 1971, A&A, 14, 252

Bilous A. V., et al., 2014, A&A, 572, A52

Bilous A. V., et al., 2016, A&A, 591, A134

Boulanger F., et al., 2018, J. Cosmology Astropart. Phys., 8, 049

Boyles J., et al., 2013, ApJ, 763, 80

Brentjens M. A., de Bruyn A. G., 2005, A&A, 441, 1217

Breton R. P., et al., 2013, ApJ, 769, 108

Brinkman C., Freire P. C. C., Rankin J., Stovall K., 2018, MNRAS, 474, 2012

Brown J. C., Taylor A. R., Wielebinski R., Mueller P., 2003, ApJ, 592, L29

Brown J. C., Haverkorn M., Gaensler B. M., Taylor A. R., Bizunok N. S., McClure-Griffiths N. M., Dickey J. M., Green A. J., 2007, ApJ, 663, 258

Burn B. J., 1966, MNRAS, 133, 67

Coenen T., et al., 2014, A&A, 570, A60

Cordes J. M., Lazio T. J. W., 2002, ArXiv Astrophysics e-prints,

Crutcher R. M., 2012, ARA&A, 50, 29

Crutcher R. M., Wandelt B., Heiles C., Falgarone E., Troland T. H., 2010, ApJ, 725, 466

Dach R., Schaer S., Arnold D., Prange L., Sidorov D., Stebler P., Villiger A., Jäggi A., 2018, Astronomical Institute, University of Bern,

Dai S., et al., 2015, MNRAS, 449, 3223

Deller A. T., et al., 2018, preprint, (arXiv:1808.09046)

Dickinson C., 2018, Galaxies, 6, 56

Dobbs C. L., Price D. J., Pettitt A. R., Bate M. R., Tricco T. S., 2016, MNRAS, 461, 4482

Farrar G. R., Jansson R., Feain I. J., Gaensler B. M., 2013, J. Cosmology Astropart. Phys., 1, 23

Ferrière K., 2011, Mem. Soc. Astron. Italiana, 82, 824

Ferrière K., Terral P., 2014, A&A, 561, A100

Force M. M., Demorest P., Rankin J. M., 2015, MNRAS, 453, 4485

Gaensler B. M., Madsen G. J., Chatterjee S., Mao S. A., 2008, Publ. Astron. Soc. Australia, 25, 184

George S. J., Stil J. M., Keller B. W., 2012, Publ. Astron. Soc. Australia, 29, 214

Geyer M., et al., 2017, MNRAS, 470, 2659

Hall J. S., 1949, Science, 109, 166

Hamilton P. A., Lyne A. G., 1987, MNRAS, 224, 1073

Han J. L., Manchester R. N., Qiao G. J., 1999, MNRAS, 306, 371

Han J. L., Manchester R. N., Lyne A. G., Qiao G. J., van Straten W., 2006, ApJ, 642, 868

Han J., et al., 2015, Advancing Astrophysics with the Square Kilometre Array (AASKA14), p. 41

Han J. L., Manchester R. N., van Straten W., Demorest P., 2018, ApJS, 234, 11

Hankins T. H., Rankin J. M., 2010, AJ, 139, 168

Haverkorn M., 2015, in Lazarian A., de Gouveia Dal Pino E. M., Melioli C., eds, Astrophysics and Space Science Library Vol. 407, Astrophysics and Space Science Library. p. 483 (arXiv:1406.0283), doi:10.1007/978-3-662-44625-6_17

Haverkorn M., Katgert P., de Bruyn A. G., 2004, A&A, 427, 169

Haverkorn M., Gaensler B. M., Brown J. C., Bizunok N. S., McClure-Griffiths N. M., Dickey J. M., Green A. J., 2006, ApJ, 637, L33

Haverkorn M., et al., 2015, Advancing Astrophysics with the Square Kilometre Array (AASKA14), p. 96

Heald G., Braun R., Edmonds R., 2009, A&A, 503, 409

Heald G., McKean J., Pizzo R., eds, 2018, Low Frequency Radio Astronomy and the LOFAR Observatory. Springer International Publishing, doi:10.1007/978-3-319-23434-2

Hermsen W., et al., 2013, Science, 339, 436

Hermsen W., et al., 2018, MNRAS, 480, 3655

Hernández-Pajares M., et al., 2009, Journal of Geodesy, 83, 263

Hiltner W. A., 1949, Science, 109, 165

Hotan A. W., van Straten W., Manchester R. N., 2004, Publ. Astron. Soc. Australia, 21, 302

Howard T. A., Stovall K., Dowell J., Taylor G. B., White S. M., 2016, The Astrophysical Journal, 831, 208

Hummel E., Beck R., Dahlem M., 1991, A&A, 248, 23

Hunter J. D., 2007, Computing In Science & Engineering, 9, 90

Jaffe T. R., Leahy J. P., Banday A. J., Leach S. M., Lowe S. R., Wilkinson A., 2010, MNRAS, 401, 1013

Jaffe T. R., Banday A. J., Leahy J. P., Leach S., Strong A. W., 2011, MNRAS, 416, 1152

Jansson R., Farrar G. R., 2012, ApJ, 761, L11

Jarvis M., et al., 2016, in Proceedings of MeerKAT Sci-

ence: On the Pathway to the SKA. 25-27 May, 2016 Stellenbosch, South Africa (MeerKAT2016). Online at https://pos.sissa.it/cgi-bin/reader/conf.cgi?confid=277, id.6. p. 6 (`arXiv:1709.01901`)

Jelić V., et al., 2015, A&A, 583, A137

Jennings R. J., Kaplan D. L., Chatterjee S., Cordes J. M., Deller A. T., 2018, ApJ, 864, 26

Johnston S., Kerr M., 2018, MNRAS, 474, 4629

Johnston-Hollitt M., et al., 2015, Advancing Astrophysics with the Square Kilometre Array (AASKA14), p. 92

Johnston S., Hobbs G., Vigeland S., Kramer M., Weisberg J. M., Lyne A. G., 2005, MNRAS, 364, 1397

Johnston S., Kramer M., Karastergiou A., Hobbs G., Ord S., Wallman J., 2007, MNRAS, 381, 1625

Johnston S., Karastergiou A., Mitra D., Gupta Y., 2008, MNRAS, 388, 261

Keane E. F., 2018, in Weltevrede P., Perera B. B. P., Preston L. L., Sanidas S., eds, IAU Symposium Vol. 337, Pulsar Astrophysics the Next Fifty Years. pp 158–164 (`arXiv:1711.01910`), doi:10.1017/S1743921317009188

Keane E., et al., 2015, Advancing Astrophysics with the Square Kilometre Array (AASKA14), p. 40

Kondratiev V. I., et al., 2016, A&A, 585, A128

Krause M., et al., 2018, A&A, 611, A72

Lazarus P., Karuppusamy R., Graikou E., Caballero R. N., Champion D. J., Lee K. J., Verbiest J. P. W., Kramer M., 2016, MNRAS, 458, 868

Lenc E., et al., 2016, ApJ, 830, 38

Lenc E., et al., 2017, Publ. Astron. Soc. Australia, 34, e040

Lynch R. S., et al., 2013, ApJ, 763, 81

Lyne A. G., Pritchard R. S., Graham-Smith F., 1993, MNRAS, 265, 1003

Lyne A. G., et al., 2017, ApJ, 834, 137

Malins J. B., White S. M., Taylor G. B., Stovall K., Dowell J., 2018, Radio Science, 53, 724

Manchester R. N., 1972, ApJ, 172, 43

Manchester R. N., 1974, ApJ, 188, 637

Manchester R. N., Taylor J. H., Huguenin G. R., 1975, ApJ, 196, 83

Manchester R. N., Hobbs G. B., Teoh A., Hobbs M., 2005, AJ, 129, 1993

Mao S. A., Gaensler B. M., Haverkorn M., Zweibel E. G., Madsen G. J., McClure-Griffiths N. M., Shukurov A., Kronberg P. P., 2010, ApJ, 714, 1170

Mao S. A., et al., 2012, ApJ, 755, 21

Michilli D., et al., 2018a, MNRAS, 476, 2704

Michilli D., et al., 2018b, MNRAS, 480, 3457

Michilli D., et al., 2018c, Nature, 553, 182

Mitra D., Wielebinski R., Kramer M., Jessner A., 2003, A&A, 398, 993

Neld A., et al., 2018, A&A, 617, A136

Ng C., et al., 2014, MNRAS, 439, 1865

Nota T., Katgert P., 2010, A&A, 513, A65

Noutsos A., Johnston S., Kramer M., Karastergiou A., 2008, MNRAS, 386, 1881

Noutsos A., Karastergiou A., Kramer M., Johnston S., Stappers B. W., 2009, MNRAS, 396, 1559

Noutsos A., et al., 2015, A&A, 576, A62

Oppermann N., et al., 2012, A&A, 542, A93

Oppermann N., et al., 2015, A&A, 575, A118

Paragi Z., et al., 2015, Advancing Astrophysics with the Square Kilometre Array (AASKA14), p. 143

Pilia M., et al., 2016, A&A, 586, A92

Planck Collaboration et al., 2016, A&A, 596, A105

Polzin E. J., et al., 2018, MNRAS, 476, 1968

Radhakrishnan V., Cooke D. J., 1969, Astrophys. Lett., 3, 225

Rand R. J., Kulkarni S. R., 1989, ApJ, 343, 760

Rand R. J., Lyne A. G., 1994, MNRAS, 268, 497

Riseley C. J., et al., 2018, Publ. Astron. Soc. Australia, 35, e043

Robishaw T., et al., 2015, Advancing Astrophysics with the Square Kilometre Array (AASKA14), p. 110

Savage B. D., Wakker B. P., 2009, ApJ, 702, 1472

Schnitzeler D. H. F. M., 2012, MNRAS, 427, 664

Schnitzeler D. H. F. M., Lee K. J., 2015, MNRAS, 447, L26

Schnitzeler D. H. F. M., Lee K. J., 2017, MNRAS, 466, 378

Schnitzeler D. H. F. M., Katgert P., de Bruyn A. G., 2007, A&A, 471, L21

Schnitzeler D. H. F. M., Katgert P., de Bruyn A. G., 2009, A&A, 494, 611

Sobey C., 2015, PhD thesis, University of Bonn

Sobey C., et al., 2015, MNRAS, 451, 2493

Sotomayor-Beltran C., et al., 2013, A&A, 552, A58

Stappers B. W., et al., 2011, A&A, 530, A80

Stovall K., et al., 2014, ApJ, 791, 67

Stovall K., et al., 2015, The Astrophysical Journal, 808, 156

Sun X.-H., Reich W., 2010, Research in Astronomy and Astrophysics, 10, 1287

Sun X. H., Reich W., 2012, A&A, 543, A127

Sun X. H., Reich W., Waelkens A., Enßlin T. A., 2008, A&A, 477, 573

Sun X. H., et al., 2015, ApJ, 811, 40

Tan C. M., et al., 2018, ApJ, 866, 54

Taylor J. H., Cordes J. M., 1993, ApJ, 411, 674

Taylor J. H., Manchester R. N., Lyne A. G., 1993, ApJS, 88, 529

Taylor G. B., et al., 2012, Journal of Astronomical Instrumentation, 1, 50004

Terral P., Ferrière K., 2017, A&A, 600, A29

Thébault E., et al., 2015, Earth, Planets and Space, 67, 79

Tiburzi C., Verbiest J. P. W., 2018, in Weltevrede P., Perera B. B. P., Preston L. L., Sanidas S., eds, IAU Symposium Vol. 337, Pulsar Astrophysics the Next Fifty Years. pp 279–282 (`arXiv:1804.04040`), doi:10.1017/S1743921317009760

Tingay S. J., et al., 2013, Publ. Astron. Soc. Australia, 30, 7

Van Eck C. L., et al., 2011, ApJ, 728, 97

Van Eck C. L., et al., 2017, A&A, 597, A98

Van Eck C. L., et al., 2018, A&A, 613, A58

Wang C., Han J. L., Lai D., 2011, MNRAS, 417, 1183

Weisberg J. M., Cordes J. M., Kuan B., Devine K. E., Green J. T., Backer D. C., 2004, ApJS, 150, 317

Xue M., et al., 2017, Publ. Astron. Soc. Australia, 34, e070

Yao J. M., Manchester R. N., Wang N., 2017, ApJ, 835, 29

van Haarlem M. P., et al., 2013, A&A, 556, A2

van Leeuwen J., Stappers B. W., 2010, A&A, 509, A7

van Straten W., Bailes M., 2011, Publ. Astron. Soc. Australia, 28, 1

APPENDIX A: SUMMARY OF OBSERVATIONS AND RESULTS

Table A1 summarises the pulsar observations in the 'slow' (non-recycled) pulsar and MSP LOFAR HBA censuses (Bilous et al. 2016; Kondratiev et al. 2016, respectively). Columns 1–4 show published information for the pulsars: the pulsar name (based on B1950 or J2000 coordinates); and the RM published in the latest version of the pulsar catalogue (v 1.59), with uncertainty ($\pm$), and literature reference (all noted by an asterisk if no literature measurements are published in the pulsar catalogue). The pulsars are listed in order of RA (as used in the pulsar catalogue), with the pulsars in the 'slow' pulsar census listed first and the pulsars in the MSP census listed after. Columns 5–9 provide the details of the LOFAR observations: modified Julian date of the LOFAR observation (MJD); signal-to-noise (S/N) of the total intensity (Stokes I) pulsar profile; number of bins used to extract the Stokes parameters from the pulse profile, and the total number of pulse profile phase bins, separated by '/'; the LOFAR DM and uncertainty (Bilous et al. 2016; Kondratiev et al. 2016). Columns 10–18 show the results from this work: the total observed RM (RM_{obs}), plus uncertainty; the ionospheric RM (RM_{ion}), plus uncertainty; RM due to the ISM alone ($RM_{ISM} = RM_{obs} - RM_{ion}$), plus uncertainty; resulting electron density-weighted average magnetic field parallel to the LoS ($\langle B_{\parallel} \rangle$), plus uncertainty; and RM dispersion output from RM CLEAN (σ_{RM}).

The references in Table A1 are listed in full in alphabetical order in Table A2, along with the number of pulsars in common with this work (MSPs are identified separately), the lowest centre observing frequency, and whether the RMs were corrected for RM_{ion}.

Table A1: Summary of RM measurements. See text for further description of columns.

PSR	RM$_{cat}$ rad m^{-2}	± rad m^{-2}	ref	MJD	S/N	Bins	DM pc cm^{-3}	± pc cm^{-3}	RM$_{obs}$ rad m^{-2}	± rad m^{-2}	RM$_{ion}$ rad m^{-2}	± rad m^{-2}	RM$_{ISM}$ rad m^{-2}	± rad m^{-2}	$\langle B_\parallel \rangle$ µG	± µG	σ$_{RM}$ rad m^{-2}
'Slow' census	= 117																
B0011+47	−15.30	0.70	hmvd18	56773.46	36	11/1024	30.4050	0.0130	−13.06	0.03	2.50	0.09	−15.56	0.10	−0.631	0.005	<0.0005
B0037+56	9.00	13.00	rl94	56753.42	38	43/1024	92.5146	0.0025	18.96	0.08	3.65	0.16	15.31	0.18	0.204	0.003	<0.0003
B0045+33	*	*	*	56703.61	98	6/1024	39.9220	0.0150	−80.14	0.02	3.14	0.09	−83.27	0.10	−2.570	0.004	<0.0005
B0052+51	−66.60	1.50	hmvd18	56776.32	35	7/1024	44.0127	0.0024	−61.69	0.03	2.40	0.06	−64.09	0.07	−1.794	0.002	<0.2227
B0053+47	−23.00	22.00	mwkj03	56703.59	19	51/1024	18.1354	0.0013	−31.38	0.10	2.78	0.09	−34.16	0.13	−2.321	0.011	<0.0004
B0105+65	−29.00	3.00	man74	56784.4	88	5/1024	30.5482	0.0014	−24.37	0.01	2.71	0.11	−27.09	0.11	−1.092	0.005	<0.0241
B0105+68	−46.00	19.00	mwkj03	56703.62	29	5/1024	61.0617	0.0036	−30.52	0.02	2.51	0.08	−33.04	0.08	−0.667	0.002	<0.1386
J0137+1654	*	*	*	56703.64	18	17/1024	26.0838	0.0024	−13.39	0.03	3.44	0.09	−16.83	0.10	−0.795	0.006	<0.0003
B0136+57	−94.13	0.08	nsk+15	56753.45	394	5/256	73.8114	0.0008	−90.26	0.01	3.71	0.19	−93.97	0.19	−1.568	0.004	<0.2819
J0152+0948	20.00	12.00	hmvd18	56784.43	12	13/1024	22.8810	0.0120	5.52	0.11	4.16	0.15	1.37	0.19	0.074	0.012	<0.0005
B0153+39	−46.50	5.50	hmvd18	56773.5	20	9/1024	59.8330	0.0110	−65.86	0.02	2.72	0.08	−68.58	0.09	−1.412	0.002	<0.1039
J0212+5222	*	*	*	56773.52	23	3/1024	38.2356	0.0005	−11.15	0.02	2.53	0.08	−13.68	0.08	−0.441	0.003	<0.1114
B0226+70	−56.00	21.00	mwkj03	56703.68	21	5/1024	46.6794	0.0016	−41.56	0.02	2.25	0.06	−43.81	0.06	−1.156	0.002	<0.0003
B0301+19	−8.30	0.30	man74	56703.69	146	2/1024	15.6568	0.0004	−5.48	0.02	2.95	0.06	−8.43	0.06	−0.663	0.006	<0.1734
B0320+39	56.30	1.00	fdr15	56703.72	625	1/1024	26.1898	0.0009	62.32	0.02	2.33	0.04	59.99	0.05	2.822	0.003	<0.3189
B0331+45	−41.00	20.00	rl94	56747.65	143	3/512	47.1457	0.0003	10.57	0.05	4.98	0.08	5.60	0.09	0.146	0.003	0.0000
B0402+61	9.00	3.00	hl87	56747.67	48	2/1024	65.4053	0.0034	12.56	0.02	4.38	0.08	8.18	0.08	0.154	0.002	<0.3028
B0410+69	−31.60	4.80	hmvd18	56773.55	77	3/1024	27.4460	0.0004	−19.09	0.02	2.33	0.06	−21.42	0.06	−0.962	0.004	0.0000
J0417+35	*	*	*	56773.56	31	4/1024	48.5336	0.0012	45.04	0.06	3.03	0.07	42.01	0.10	1.066	0.003	<0.0004
J0435+2749	2.00	0.00	bfrs18	56773.58	20	9/512	53.1819	0.0002	4.21	0.07	3.25	0.06	0.96	0.09	0.022	0.003	<0.0005
B0450+55	10.00	3.00	hl87	56772.61	275	1/1024	14.5900	0.0002	8.74	0.01	2.94	0.11	5.79	0.11	0.489	0.011	<0.0004
B0523+11	37.00	2.00	jhv+05	56703.77	32	28/512	79.4180	0.0130	22.18	0.13	2.07	0.10	20.11	0.17	0.312	0.003	0.0000
B0525+21	−39.60	0.20	man72	56747.71	746	1/1024	50.8695	0.0013	−34.55	0.01	5.47	0.06	−40.02	0.07	−0.969	0.002	<0.2558
B0531+21	−42.30	0.50	man72	56703.78	120	1/64	56.7712	0.0002	−43.70	0.01	1.74	0.08	−45.44	0.08	−0.986	0.002	<0.2542
B0540+23	2.70	0.60	jkk+07	56779.57	39	1/256	77.7026	0.0010	5.95	0.01	3.10	0.10	2.85	0.10	0.045	0.002	<0.1797
J0611+30	*	*	*	56772.64	78	2/1024	45.2551	0.0016	17.91	0.02	3.45	0.08	14.46	0.08	0.394	0.003	0.0000
B0609+37	23.00	9.00	wck+04	56772.66	50	1/512	27.1550	0.0003	37.73	0.02	3.22	0.05	34.51	0.06	1.566	0.003	<0.0005
B0626+24	69.50	0.20	wck+04	56747.76	160	2/512	84.1762	0.0050	80.41	0.02	4.70	0.09	75.70	0.09	1.108	0.002	<0.2716
B0643+80	−32.00	3.00	hl87	56747.78	97	1/1024	33.3188	0.0007	−28.87	0.01	2.89	0.06	−31.77	0.07	−1.175	0.003	<0.2068
B0656+14	23.00	0.30	jkk+07	56747.75	15	14/1024	14.0762	0.0024	28.00	0.02	5.26	0.07	22.73	0.08	1.990	0.008	<0.0004
B0655+64	−7.00	6.00	hl87	56772.68	112	3/1024	8.7739	0.0003	−15.36	0.02	2.71	0.06	−18.07	0.06	−2.537	0.011	<0.0003
B0751+32	−7.00	5.00	hl87	56772.72	104	11/1024	39.9863	0.0014	7.60	0.03	3.42	0.08	4.18	0.09	0.129	0.003	<0.1472
B0809+74	−14.00	0.07	nsk+15	56747.8	661	2/1024	5.7507	0.0005	−11.07	0.01	2.84	0.06	−13.91	0.06	−2.980	0.016	<0.1743
B0823+26	5.38	0.06	nsk+15	56747.82	1589	2/1024	19.4763	0.0002	8.93	0.01	3.87	0.10	5.05	0.10	0.320	0.008	<0.0953
B0841+80	−23.20	3.10	hmvd18	56747.83	23	7/1024	34.8121	0.0031	−19.42	0.03	2.36	0.04	−21.78	0.05	−0.771	0.002	<0.0004
B0917+63	−18.90	2.30	hmvd18	56747.89	164	2/1024	13.1542	0.0002	−12.81	0.01	2.12	0.06	−14.93	0.06	−1.399	0.007	<0.1745
B0940+16	53.00	12.00	hl87	56687.1	21	2/1024	20.3402	0.0018	18.23	0.02	0.86	0.06	17.36	0.07	1.052	0.005	0.0000
J0943+2253	*	*	*	56747.86	33	3/1024	27.2676	0.0016	19.76	0.02	3.33	0.08	16.43	0.08	0.742	0.004	<0.0004
B0943+10	13.30	0.50	tml93	56779.82	882	1/1024	15.3185	0.0009	17.23	0.02	3.13	0.08	14.10	0.08	1.134	0.008	<0.1470
J0947+2740	32.00	0.00	bfrs18	56747.88	24	5/1024	28.8860	0.0260	26.28	0.02	3.03	0.06	23.25	0.06	0.992	0.003	<0.1104
B1112+50	−0.10	0.80	fdr15	56747.93	150	5/1024	9.1863	0.0003	4.44	0.01	2.02	0.07	2.41	0.07	0.324	0.012	<0.1194
B1133+16	3.97	0.07	nsk+15	56687.11	2220	1/1024	4.8407	0.0003	5.00	0.01	0.89	0.06	4.11	0.06	1.046	0.019	<0.0005
J1238+2152	*	*	*	56687.14	133	2/1024	17.9706	0.0031	5.21	0.01	0.80	0.05	4.41	0.06	0.303	0.005	<0.1848
J1246+2253	*	*	*	56747.99	21	29/1024	17.7978	0.0018	6.01	0.03	2.42	0.09	3.59	0.09	0.248	0.008	<0.0004
J1313+0931	*	*	*	56779.92	152	1/1024	12.0406	0.0000	4.49	0.02	2.17	0.10	2.32	0.11	0.237	0.013	<0.1704
B1322+83	−23.20	1.10	fdr15	56687.19	90	1/1024	13.3162	0.0008	−23.32	0.02	0.35	0.05	−23.67	0.05	−2.190	0.005	<0.0005
B1508+55	1.28	0.06	nsk+15	56687.26	3384	1/1024	19.6189	0.0013	2.04	0.01	0.55	0.06	1.49	0.06	0.094	0.005	<0.1733
B1530+27	1.00	0.30	wck+04	56703.26	72	7/1024	14.6910	0.0160	4.26	0.02	0.89	0.08	3.37	0.08	0.283	0.008	<0.1293
B1541+09	21.00	2.00	hl87	56780.02	544	1/1024	34.9758	0.0016	17.61	0.01	1.66	0.09	15.95	0.09	0.562	0.004	<0.1028
J1612+2008	22.00	3.00	blr+13	56687.25	15	9/1024	19.5082	0.0032	23.01	0.02	0.75	0.06	22.26	0.07	1.406	0.005	0.0000
J1627+1419	18.30	5.90	hmvd18	56687.29	64	1/1024	32.1670	0.0008	19.85	0.02	1.24	0.06	18.61	0.06	0.713	0.003	<0.0009
B1633+24	31.00	4.00	wck+04	56748.14	135	2/1024	24.2671	0.0044	23.81	0.03	1.85	0.06	21.97	0.07	1.115	0.004	<0.0003
J1645+1012	*	*	*	56687.33	87	1/1024	36.1713	0.0002	32.25	0.02	2.05	0.10	30.20	0.10	1.029	0.004	0.0000
J1649+2533	29.70	1.00	hmvd18	56748.12	25	11/1024	34.4622	0.0078	31.39	0.03	1.87	0.05	29.52	0.06	1.055	0.003	<0.0987
J1652+2651	34.50	0.70	hmvd18	56748.11	33	21/1024	40.8024	0.0002	35.56	0.07	1.85	0.04	33.71	0.08	1.018	0.003	<0.1472
Continued on next page																	

Table A1 – continued from previous page

PSR	RM$_{cat}$ rad m^{-2}	± rad m^{-2}	ref	MJD	S/N	Bins	DM pc cm^{-3}	± pc cm^{-3}	RM$_{obs}$ rad m^{-2}	± rad m^{-2}	RM$_{ion}$ rad m^{-2}	± rad m^{-2}	RM$_{ISM}$ rad m^{-2}	± rad m^{-2}	$\langle B_\parallel \rangle$ μG	± μG	σ_{RM} rad m^{-2}
J1720+2150	50.00	3.70	hmvd18	56748.15	16	5/1024	40.7190	0.0350	54.76	0.03	1.82	0.06	52.94	0.07	1.602	0.003	<0.1456
B1737+13	64.40	1.60	wck+04	56687.3	161	2/1024	48.6682	0.0004	68.22	0.03	1.58	0.07	66.65	0.08	1.687	0.002	<0.0005
J1741+2758	49.90	5.70	hmvd18	56773.14	93	5/1024	29.1449	0.0001	56.03	0.03	1.34	0.06	54.70	0.07	2.312	0.004	0.0000
J1746+2245	68.70	3.70	hmvd18	56784.14	25	3/1024	49.8543	0.0057	73.84	0.08	1.57	0.10	72.28	0.12	1.786	0.004	<0.0003
J1746+2540	93.20	1.50	hmvd18	56784.17	13	13/1024	51.2044	0.0033	96.46	0.08	1.71	0.10	94.75	0.12	2.280	0.004	<0.0003
J1752+2359	*	*	*	56783.18	20	9/1024	36.1964	0.0006	88.64	0.06	1.59	0.09	87.05	0.11	2.963	0.005	<0.0005
B1753+52	26.60	1.10	hmvd18	56785.18	17	5/1024	35.0096	0.0064	29.25	0.08	1.31	0.07	27.94	0.11	0.983	0.005	<0.0672
J1758+3030	70.40	2.20	hmvd18	56784.19	157	4/1024	35.0674	0.0014	81.39	0.07	1.85	0.10	79.54	0.12	2.794	0.005	<0.0005
B1811+40	47.00	6.00	hl87	56780.05	103	2/1024	41.5566	0.0002	50.53	0.02	1.15	0.06	49.38	0.06	1.464	0.002	<0.1568
J1821+1715	107.50	1.20	hmvd18	56703.3	25	7/1024	60.2844	0.0025	111.21	0.08	1.85	0.10	109.36	0.13	2.235	0.003	<0.0665
J1838+1650	66.50	2.70	hmvd18	56801.09	84	1/1024	32.9516	0.0010	74.36	0.02	1.71	0.12	72.65	0.12	2.716	0.005	<0.0772
B1839+56	−5.00	0.70	fdr15	56789.09	532	1/1024	26.7716	0.0002	−2.58	0.01	1.27	0.06	−3.85	0.06	−0.177	0.004	<0.0917
B1839+09	53.00	5.00	hl87	56783.19	110	1/1024	49.1579	0.0043	53.23	0.02	2.04	0.10	51.19	0.10	1.283	0.003	<0.1000
B1842+14	109.00	1.30	jhv+05	56703.31	145	3/1024	41.4856	0.0006	120.84	0.04	2.19	0.11	118.65	0.12	3.524	0.004	<0.1303
J1849+2423	12.80	1.20	hmvd18	56788.06	9	4/512	62.2677	0.0016	16.82	0.03	1.64	0.05	15.18	0.06	0.300	0.001	<0.0005
B1848+13	152.70	0.60	jkk+07	56703.14	10	11/512	60.1396	0.0066	157.58	0.10	2.65	0.12	154.93	0.16	3.174	0.004	<0.0005
B1848+12	158.00	16.00	rl94	56687.43	53	3/1024	70.6333	0.0017	152.53	0.03	2.73	0.12	149.80	0.12	2.613	0.003	<0.2659
B1905+39	5.20	0.30	fdr15	56789.13	119	1/1024	30.9660	0.0140	6.88	0.01	1.47	0.08	5.41	0.09	0.215	0.004	<0.1029
J1912+2525	12.30	7.00	hmvd18	56788.23	42	2/1024	37.8474	0.0016	34.69	0.02	2.04	0.09	32.65	0.10	1.063	0.004	<0.0621
B1918+26	20.30	1.30	hmvd18	56748.21	95	2/1024	27.7088	0.0008	28.11	0.02	2.07	0.07	26.04	0.07	1.158	0.004	<0.0005
B1919+21	−16.99	0.05	nsk+15	56788.21	2054	1/1024	12.4440	0.0006	−15.04	0.02	2.01	0.10	−17.05	0.10	−1.688	0.012	<0.0005
B1929+10	−6.87	0.02	jhv+05	56781.21	314	1/1024	3.1832	0.0002	−5.27	0.01	1.86	0.14	−7.14	0.14	−2.762	0.065	<0.0863
B1944+17	−28.00	0.40	hl87	56801.14	29	9/1024	16.1356	0.0073	−43.64	0.02	1.70	0.10	−45.34	0.11	−3.462	0.010	<0.1774
B1946+35	116.00	6.00	hl87	56748.23	28	70/1024	129.3675	0.0008	121.07	0.09	2.11	0.06	118.96	0.11	1.133	0.001	<0.3047
B1953+50	−23.84	0.05	nsk+15	56789.06	155	1/1024	31.9827	0.0001	−22.50	0.01	1.31	0.06	−23.82	0.06	−0.918	0.003	<0.1041
J1956+0838	*	*	*	56781.27	6	25/1024	67.0870	0.0240	−111.05	0.11	2.44	0.12	−113.49	0.16	−2.084	0.004	0.0000
J2002+1637	*	*	*	56773.22	4	8/256	94.5810	0.0480	−39.29	0.09	1.98	0.10	−41.27	0.13	−0.538	0.002	<0.0004
J2007+0809	*	*	*	56779.29	10	47/512	53.3940	0.0370	−130.49	0.07	2.84	0.13	−133.32	0.15	−3.076	0.005	<0.0005
J2007+0910	−73.00	15.00	hmvd18	56784.25	36	5/1024	48.7293	0.0007	−74.57	0.09	3.24	0.09	−77.81	0.13	−1.967	0.004	0.0000
J2017+2043	−168.00	3.10	hmvd18	56772.32	32	8/1024	60.4906	0.0099	−160.93	0.03	2.68	0.09	−163.61	0.10	−3.332	0.002	<0.0004
B2016+28	−34.60	1.40	man72	56781.23	1255	1/1024	14.1839	0.0013	−33.14	0.01	1.76	0.11	−34.90	0.11	−3.032	0.012	<0.1741
B2020+28	−74.70	0.30	man74	56748.24	252	1/1024	24.6131	0.0002	−72.56	0.02	2.48	0.06	−75.04	0.06	−3.753	0.004	<0.1595
B2021+51	−6.50	0.90	man72	56789.31	126	1/1024	22.5497	0.0006	−4.31	0.01	2.42	0.08	−6.73	0.08	−0.368	0.005	<0.1258
B2022+50	42.60	1.20	hmvd18	56789.08	75	1/1024	32.9882	0.0004	46.11	0.02	1.28	0.06	44.84	0.06	1.675	0.003	<0.0005
J2036+2835	*	*	*	56801.17	23	3/1024	84.2174	0.0064	−156.45	0.03	1.69	0.12	−158.14	0.12	−2.313	0.002	<0.0006
B2034+19	−97.00	10.00	wck+04	56773.27	91	1/1024	36.8916	0.0000	−108.46	0.02	2.22	0.10	−110.69	0.10	−3.696	0.004	<0.1957
B2036+53	−102.30	1.90	hmvd18	56789.33	8	25/1024	160.1960	0.0120	−100.56	0.10	2.49	0.08	−103.05	0.13	−0.793	0.001	<0.0005
J2043+2740	*	*	*	56784.28	233	1/256	21.0206	0.0002	−93.08	0.01	3.06	0.12	−96.14	0.12	−5.635	0.009	<0.1766
B2044+15	−100.00	5.00	wck+04	56773.25	72	5/1024	39.8180	0.0005	−88.02	0.06	2.18	0.09	−90.20	0.11	−2.791	0.004	<0.0940
B2045+56	0.60	1.90	hmvd18	56789.16	54	1/512	101.7903	0.0001	2.79	0.02	1.54	0.08	1.25	0.08	0.015	0.001	<0.0005
B2053+21	−100.00	7.00	hr10	56773.34	100	1/1024	36.3496	0.0003	−86.71	0.02	2.69	0.08	−89.40	0.08	−3.030	0.003	<0.0961
J2111+2106	−75.30	0.80	blr+13	56773.31	15	9/1024	59.2964	0.0035	−72.47	0.10	2.51	0.09	−74.99	0.14	−1.558	0.003	0.0000
B2110+27	−37.00	7.00	wck+04	56784.29	425	1/1024	25.1111	0.0002	−56.95	0.02	3.23	0.13	−60.18	0.13	−2.953	0.008	0.0000
B2113+14	−25.00	8.00	hl87	56703.48	21	45/1024	56.2044	0.0061	−35.30	0.07	3.74	0.09	−39.04	0.11	−0.856	0.003	<0.0003
J2139+2242	−86.00	0.40	hmvd18	56753.38	64	1/1024	44.1597	0.0008	−83.13	0.02	4.25	0.22	−87.38	0.22	−2.438	0.008	<0.1608
B2148+63	−156.50	0.30	fdr15	56786.34	54	26/512	129.7229	0.0055	−155.62	0.03	1.98	0.09	−157.60	0.09	−1.497	0.001	<0.2486
J2155+2813	−131.80	4.50	hmvd18	56784.31	31	14/1024	77.1309	0.0043	−129.30	0.06	3.36	0.13	−132.67	0.14	−2.119	0.003	<0.1351
B2154+40	−32.60	3.00	fdr15	56687.54	321	1/1024	71.1239	0.0022	−39.68	0.01	2.35	0.12	−42.03	0.12	−0.728	0.003	<0.2118
J2205+1444	−27.50	3.40	hmvd18	56703.5	10	8/1024	36.7460	0.0620	−21.76	0.08	3.76	0.08	−25.51	0.11	−0.855	0.005	<0.0003
B2210+29	−168.00	5.00	wck+04	56784.33	36	8/1024	74.5213	0.0015	−165.23	0.07	3.44	0.12	−168.66	0.14	−2.788	0.003	<0.2767
J2215+1538	−18.70	1.00	hmvd18	56703.55	16	6/1024	29.2404	0.0012	−16.21	0.03	3.81	0.09	−20.02	0.09	−0.843	0.005	<0.0004
B2217+47	−35.93	0.06	nsk+15	56687.56	3281	1/1024	43.4862	0.0060	−33.60	0.01	2.12	0.10	−35.73	0.10	−1.012	0.004	<0.0360
J2222+2923	*	*	*	56773.4	12	8/512	49.4128	0.0011	−92.96	0.07	2.75	0.08	−95.71	0.11	−2.386	0.003	<0.0005
B2224+65	−22.99	0.07	nsk+15	56784.36	232	1/1024	36.4436	0.0005	−20.05	0.01	2.69	0.10	−22.73	0.10	−0.769	0.004	<0.1735
B2227+61	−125.00	22.00	mwkj03	56783.23	52	14/512	124.6388	0.0031	−104.22	0.03	1.69	0.09	−105.91	0.09	−1.047	0.001	<0.2237
B2241+69	−30.00	30.00	mwkj03	56784.34	67	1/1024	40.8604	0.0007	−14.16	0.02	2.64	0.09	−16.80	0.09	−0.506	0.003	<0.0005
J2253+1516	−32.00	3.00	hmvd18	56703.53	39	18/1024	29.2045	0.0017	−27.14	0.07	3.84	0.09	−30.98	0.11	−1.307	0.006	<0.0004
B2303+30	−75.50	4.00	wck+04	56773.41	215	1/1024	49.5845	0.0012	−84.27	0.03	2.77	0.10	−87.04	0.10	−2.163	0.003	<0.0697

Continued on next page

Table A2. Summary of the references for published RMs in Table A1.

Reference	N pulsars in common 'slow' + MSP	(lowest) Centre frequency (MHz)	Ionospheric RM corrected (Yes/No)
bfrs18 (Brinkman et al. 2018)	2	327	N
blr+13 (Boyles et al. 2013)	2	820	N
dhm+15 (Dai et al. 2015)	3 MSPs	730	Y
fdr15 (Force et al. 2015)	8	1100	N
hl87 (Hamilton & Lyne 1987)	14	408	Y
hmvd18 (Han et al. 2018)	32 + 4 MSPs	774	Y
hr10 (Hankins & Rankin 2010)	1	50	N
jhv+05 (Johnston et al. 2005)	3	1369	Y
jkk+07 (Johnston et al. 2007)	3	690	N
lbr+13 (Lynch et al. 2013)	1 MSP	350/820	N
man72 (Manchester 1972)	4	250	Y
man74 (Manchester 1974)	3	250	Y
mwkj03 (Mitra et al. 2003)	5	1400	N
nsk+15 (Noutsos et al. 2015)	9 + 3 MSPs	150	Y
rl94 (Rand & Lyne 1994)	3	1400	N
tml93 (Taylor et al. 1993)	1	various	various
wck+04 (Weisberg et al. 2004)	10	430	Y

Table A1 – continued from previous page

PSR	RM_{cat} rad m^{-2}	$\pm$ rad m^{-2}	ref	MJD	S/N	Bins	DM pc cm^{-3}	$\pm$ pc cm^{-3}	RM_{obs} rad m^{-2}	$\pm$ rad m^{-2}	RM_{ion} rad m^{-2}	$\pm$ rad m^{-2}	RM_{ISM} rad m^{-2}	$\pm$ rad m^{-2}	$\langle B_{\parallel} \rangle$ μG	$\pm$ μG	σ_{RM} rad m^{-2}
B2303+46	−25.00	11.00	hmvd18	56773.43	37	3/1024	62.0676	0.0036	−19.64	0.02	2.44	0.09	−22.08	0.09	−0.438	0.002	<0.0958
B2306+55	−34.00	3.00	hl87	56785.24	81	4/1024	46.5391	0.0004	−27.68	0.02	1.67	0.07	−29.35	0.08	−0.777	0.003	<0.1870
B2310+42	4.40	0.10	fdr15	56687.59	318	1/1024	17.2769	0.0003	7.03	0.01	2.06	0.09	4.97	0.09	0.355	0.008	<0.2096
B2315+21	−37.00	3.00	hl87	56687.52	257	1/1024	20.8696	0.0003	−35.28	0.01	2.67	0.13	−37.94	0.13	−2.240	0.009	<0.1231
MSP census	= 19																
J0030+0451	17.00	16.00	hmvd18	56304.694	31	6/1024	4.33261	0.00001	2.49	0.03	1.32	0.07	1.17	0.08	0.332	0.026	<0.1489
J0214+5222	*	*	*	56646.791	41	8/1024	22.03610	0.00010	−15.93	0.03	0.50	0.07	−16.44	0.07	−0.919	0.005	<0.0004
J0218+4232	*	*	*	56473.304	19	12/256	61.23890	0.00030	−59.81	0.03	1.60	0.07	−61.40	0.08	−1.235	0.002	<0.0757
J0407+1607	*	*	*	56790.515	30	13/1024	35.61091	0.00017	6.31	0.06	3.78	0.11	2.53	0.13	0.087	0.005	<0.2229
J0621+1002	28.80	6.80	hmvd18	56289.023	9	12/128	36.53490	0.00810	53.91	0.11	0.71	0.07	53.20	0.13	1.794	0.005	0.0000
J0636+5129	*	*	*	56648.046	10	6/128	11.10647	0.00021	−1.72	0.08	0.41	0.06	−2.14	0.10	−0.237	0.013	<0.0005
J0645+5158	*	*	*	56322.009	19	6/1024	18.24846	0.00015	−1.58	0.08	0.39	0.07	−1.97	0.11	−0.133	0.009	<0.0005
J1012+5307	2.98	0.06	nsk+15	56289.149	32	1/1024	9.02436	0.00008	3.38	0.02	0.39	0.06	2.98	0.06	0.407	0.010	<0.1889
J1022+1001	1.39	0.05	nsk+15	56296.126	49	3/1024	10.25327	0.00016	2.09	0.02	0.90	0.05	1.19	0.05	0.143	0.007	<0.2638
J1024−0719	−2.40	0.20	dhm+15	56280.16111	10	25/512	6.48445	0.00025	−1.89	0.06	1.06	0.07	−2.95	0.09	−0.561	0.022	<0.0005
B1257+12	7.91	0.06	nsk+15	56296.23	44	4/1024	10.15405	0.00011	8.55	0.02	0.77	0.07	7.78	0.07	0.944	0.011	<0.2084
J1640+2224	24.60	9.40	hmvd18	56289.368	15	6/512	18.42766	0.00001	24.22	0.03	1.41	0.07	22.81	0.07	1.525	0.006	<0.1926
J1744−1134	2.20	0.20	dhm+15	56293.44	15	23/512	3.13815	0.00008	4.22	0.07	2.63	0.08	1.59	0.11	0.625	0.052	<0.0005
J1810+1744	*	*	*	56293.456	65	24/512	39.66000	0.00020	90.15	0.07	1.62	0.06	88.53	0.10	2.750	0.004	<0.0004
J1923+2515	10.80	3.80	lbr+13	56318.472	12	51/512	18.85567	0.00012	15.44	0.10	3.10	0.09	12.34	0.13	0.807	0.011	0.0000
B1937+21	8.30	0.10	dhm+15	56434.134	25	1/256	71.02373	0.00005	9.45	0.02	1.72	0.06	7.73	0.06	0.134	0.001	<0.2463
J2043+1711	*	*	*	56311.522	14	3/256	20.71232	0.00019	−70.94	0.03	2.09	0.07	−73.04	0.08	−4.344	0.006	<0.1028
J2214+3000	*	*	*	56457.159	7	13/128	22.54310	0.00420	−43.13	0.11	1.79	0.08	−44.91	0.13	−2.455	0.009	<0.0005
J2317+1439	−4.00	3.30	hmvd18	56304.635	40	13/256	21.89876	0.00026	−8.40	0.01	1.53	0.07	−9.93	0.07	−0.559	0.005	<0.1760

APPENDIX B: FDF SUMMARY

Here, we present some additional results from analysis of the FDFs output by the RM synthesis method.

Figure B1 shows examples of some of the statistics output from testing the numbers of pulse phase bins used to output the Stokes parameters for the RM synthesis step. This includes the RM measured from the FDF, the S/N in the FDF (S/N_F), and the ratio between the peak signal associated with the pulsar and the peak due to the instrumental polarisation in the FDF (PSR/Inst). Figure B1 provides an example of two pulsars: one with with relatively low S/N (PSR B0045+33); and one with high S/N (PSR B0329+54). Table B1 summarises the main results from the tests. For PSR B0045+33, the RM with the highest S/N_F was used for the final results presented in this work (6 bins). Cumulative bin numbers 4–8 would also be suitable, based on $S/N_F \geqslant 8$ and PSR/Inst>1, and these measured RMs agree within the uncertainties. For PSR B0329+54, the RM value for the final catalogue was chosen based on a compromise between relatively high S/N and PSR/Inst (5 bins). However, due to the high S/N and PSR/Inst for the pulsar, we see little variation between the measured RMs, which are all in excellent agreement within the uncertainties. Table B1 shows that for pulsars with lower S/N, the standard deviation for the RMs measured using different ranges of pulse phase bins is larger than for the higher S/N case. In the low S/N case, the standard deviation is approximately equal to the formal errors output from the RM measurement in the FDF. Due to the larger variation identified in these cases, the uncertainties from the RM measurements for pulsars with $4 < S/N_F \leqslant 8$ were doubled. This increased the uncertainties for 37 pulsars in the sample, but nonetheless, the uncertainties remain relatively small – the maximum value is $0.13\,\mathrm{rad\ m^{-2}}$. The standard deviations for the instrumental signals in both low and high S/N cases are identical.

Figure B2 shows the position of the instrumental peak (ϕ_{inst}) measured from the FDFs where a significant RM was detected. The median value is $0.04\,\mathrm{rad\ m^{-2}}$, and the standard deviation is $0.25\,\mathrm{rad\ m^{-2}}$ (32 per cent of $\delta\phi$). The histogram and statistics show that the instrumental peak in the FDFs does not deviate greatly from $0\,\mathrm{rad\ m^{-2}}$. This is generally expected since instrumental polarisation is not likely to vary with observing wavelength squared.

Figure B3 presents the FDFs obtained for each pulsar summarised in Table A1, highlighting the RM_{obs} measured.
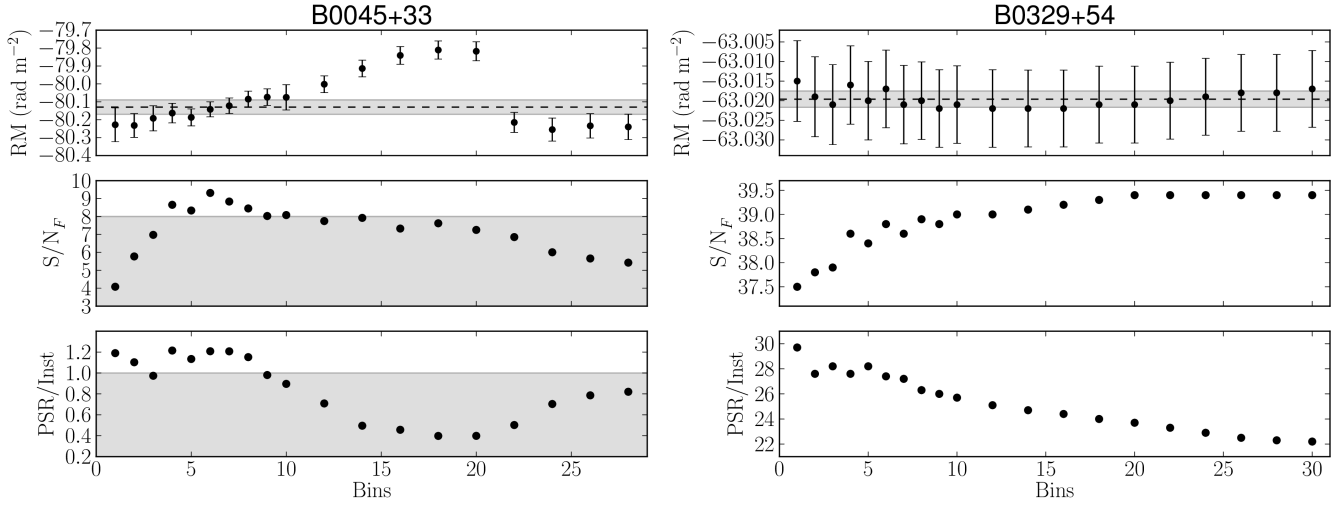
Figure B1. FDF statistics as a function of increasing numbers of pulse profile bins used to obtain the Stokes parameters from the average pulse profiles of PSR B0045+33 (left) and PSR B0329+54 (right). Top panel: measured RMs and formal uncertainties. The weighted mean RM for all measurements with $S/N_F > 8$ is shown by the dashed line, and the weighted mean $\pm$ the standard deviation of the measurements is shaded in grey. Middle panel: measured S/N of the signal associated with the pulsar in the FDFs, $S/N_F < 8$ is shown by the shaded region. Lower panel: the ratio between the intensity of the signal associated with the pulsar and the intensity of the instrumental polarisation near $0\,\mathrm{rad\,m^{-2}}$ in the FDF (PSR/Inst). The region where PSR/Inst<1 shaded.

Table B1. Summary of RM statistics (in units of $\mathrm{rad\,m^{-2}}$) from the Stokes parameters output using a range in pulse profile bin numbers, shown in Figure B1. For PSR B0045+33, the RM weighted mean and standard deviation were calculated using values with S/N>8.

Parameter	PSR B0045+33	PSR B0329+54
Pulsar RM ($\mathrm{RM_{obs}}$) weighted mean	−80.13	−63.020
Pulsar RM standard deviation	0.04	0.002
Instrumental (ϕ_{inst}) mean	−0.07	−0.33
Instrumental standard deviation	0.02	0.02

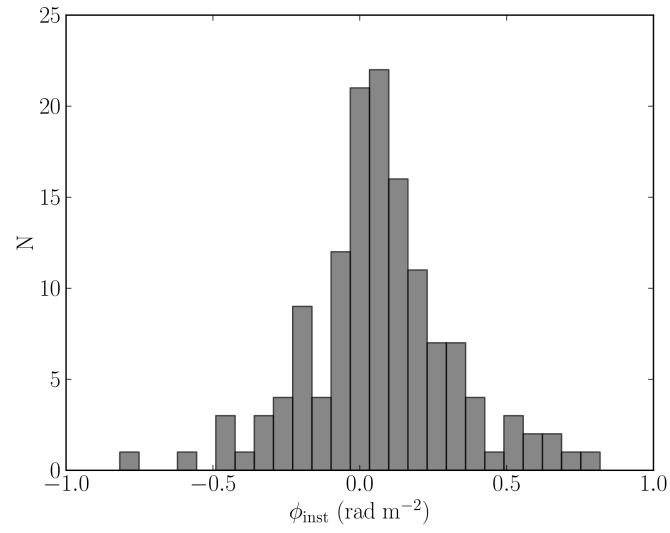This paper has been typeset from a TeX/LaTeX file prepared by the author.

Figure B2. A histogram showing the positions of the instrumental peak measured in the FDFs (ϕ_{inst}) determined for all pulsars for which we obtained an RM measurement.
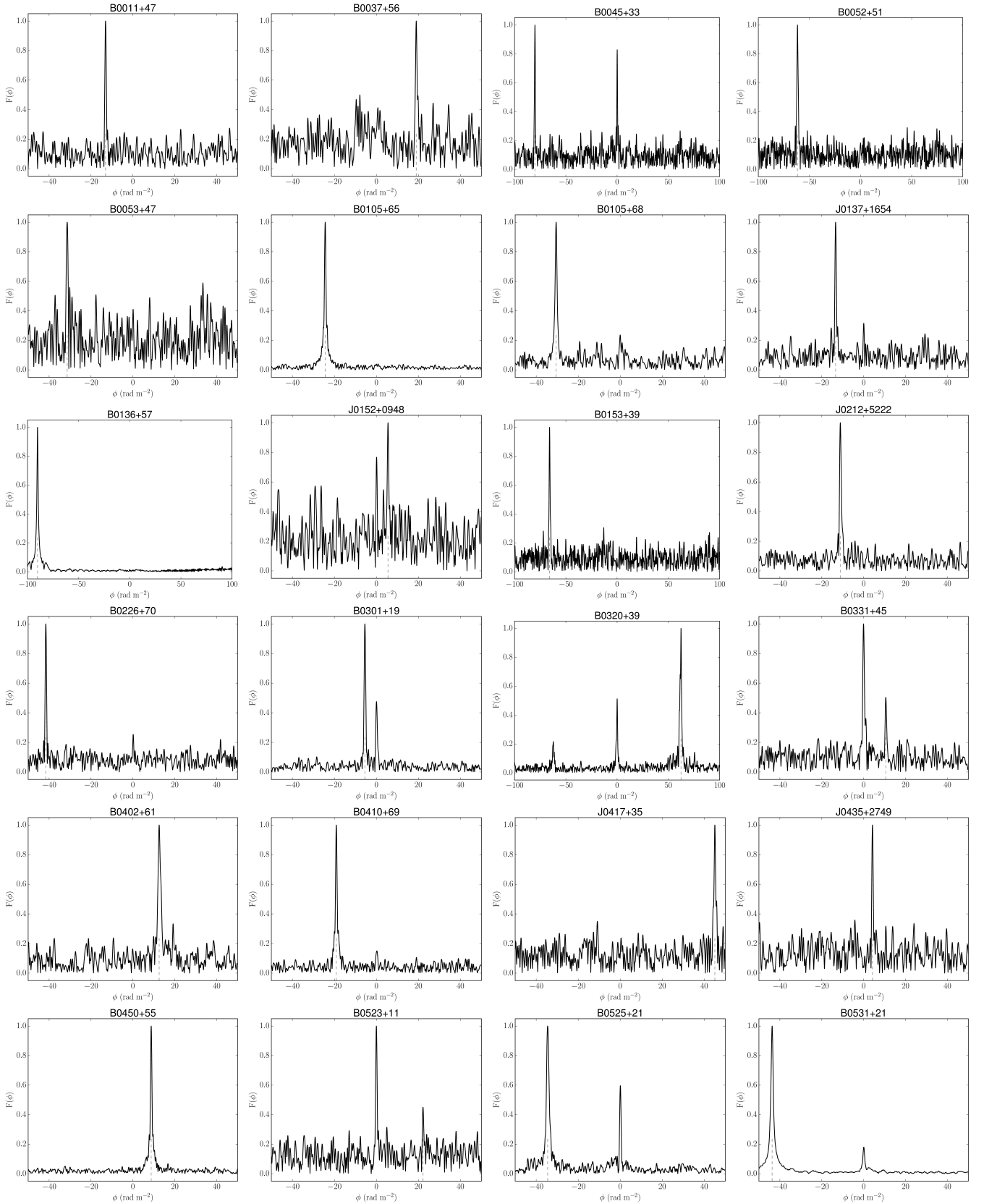
Figure B3. Faraday spectra (modulus values) for the pulsars towards which we measured an RM, ordered as in Table A1. The grey dashed line indicates the position of the peak in Faraday space, RM_{obs}, prior to any subtraction of the ionospheric RM. The x-axes show the Faraday depth between ±50, ±100, ±150, or ±200 rad m^{-2}, depending on the measured RM towards each pulsar. The y-axes show the intensity of linearly-polarised emission in arbitrary units (normalised) because the data are not flux or polarisation calibrated. Peaks near 0 rad m^{-2} are due to instrumental polarisation, and smaller symmetric peaks about 0 rad m^{-2} are due to polarisation leakage.
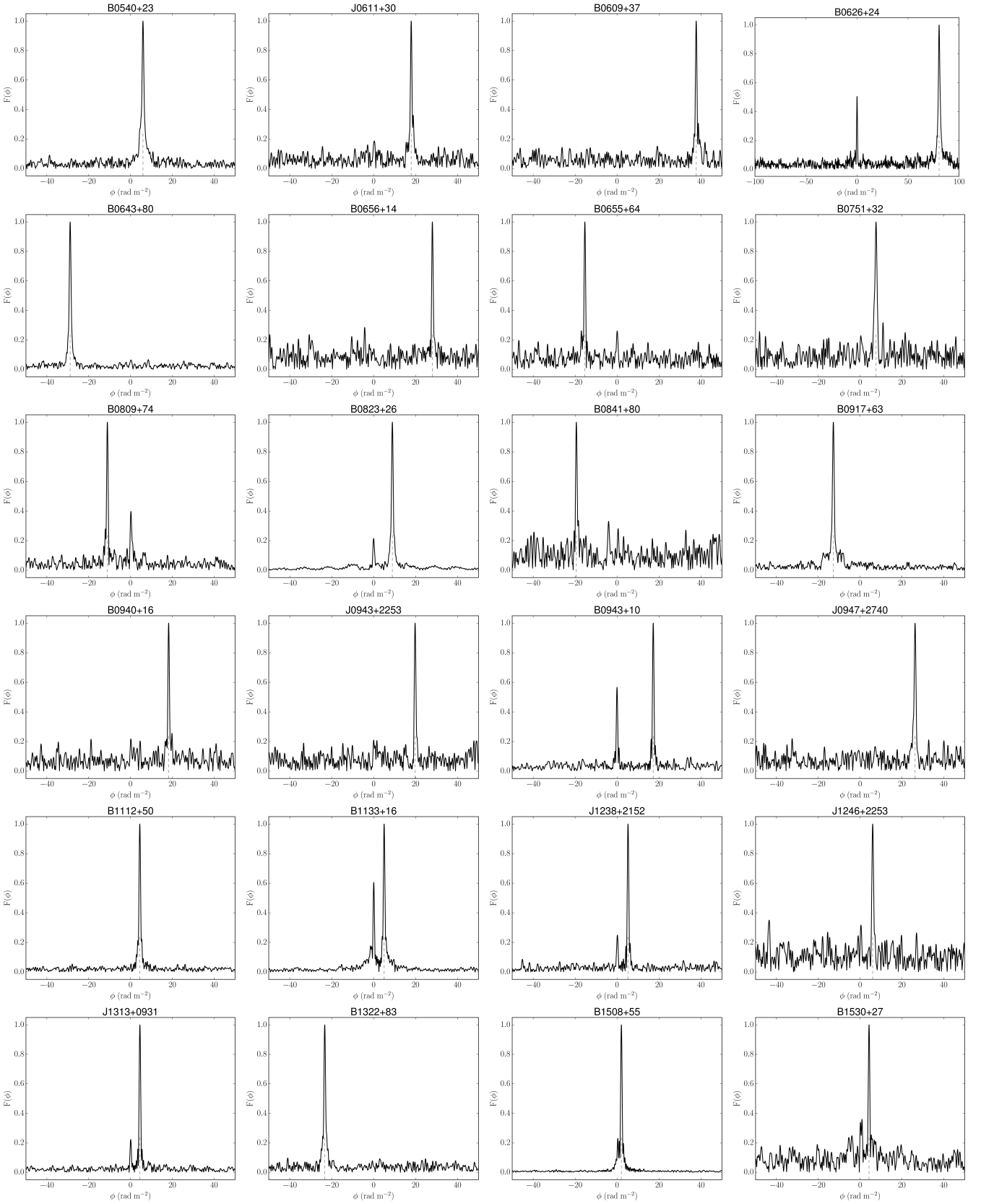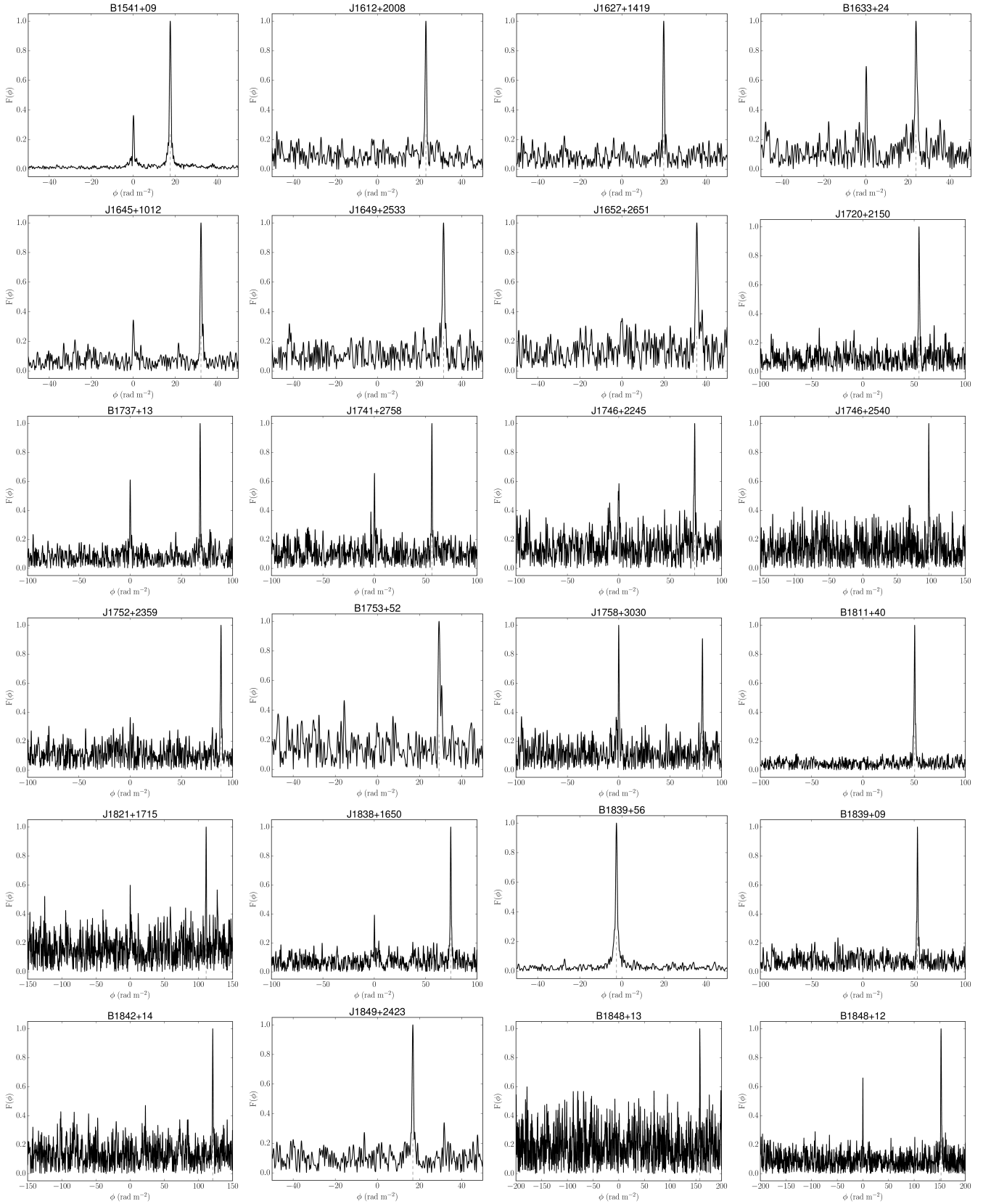
Figure B4. Continued from the previous page.

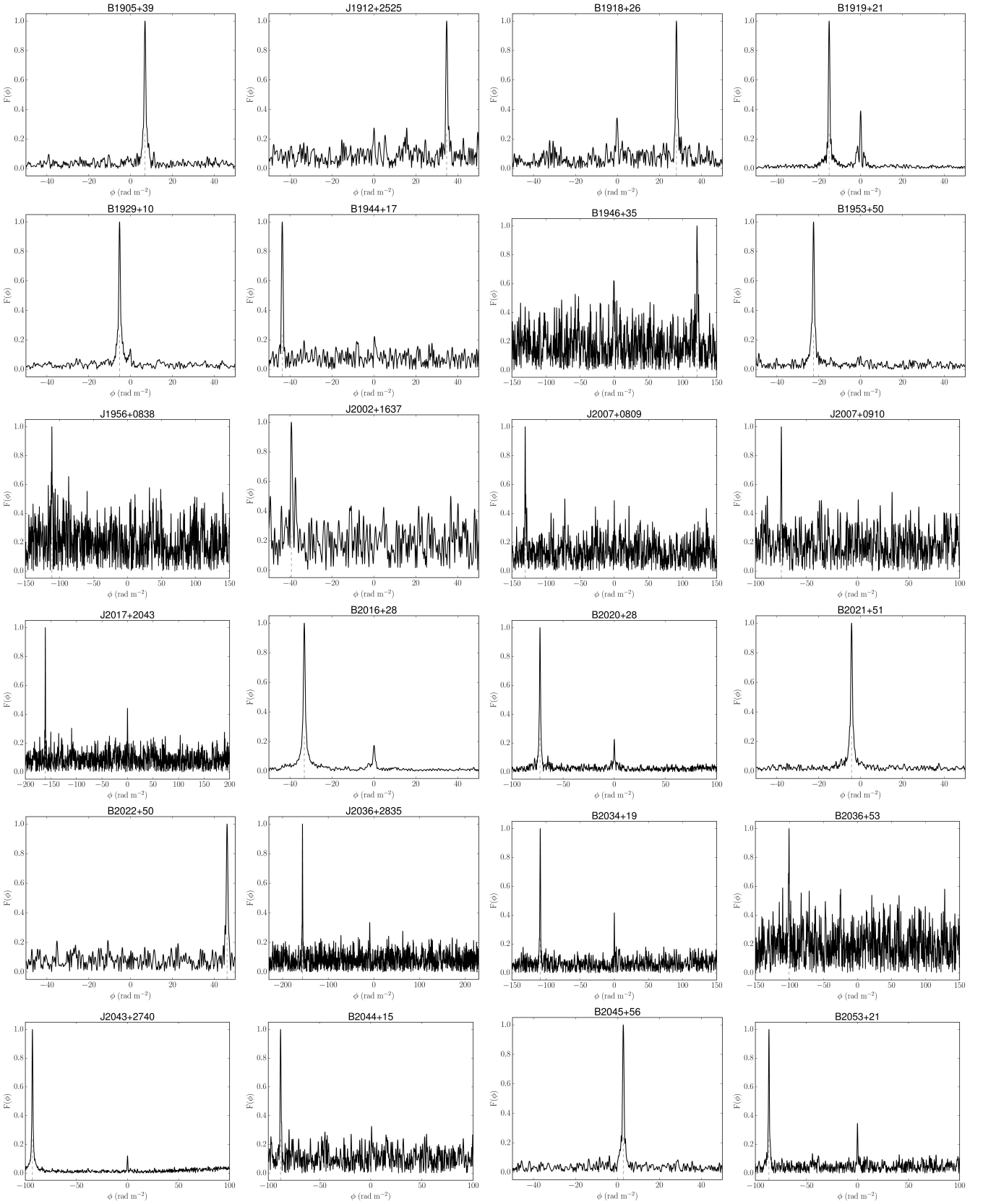**Figure B5.** Continued from the previous page.

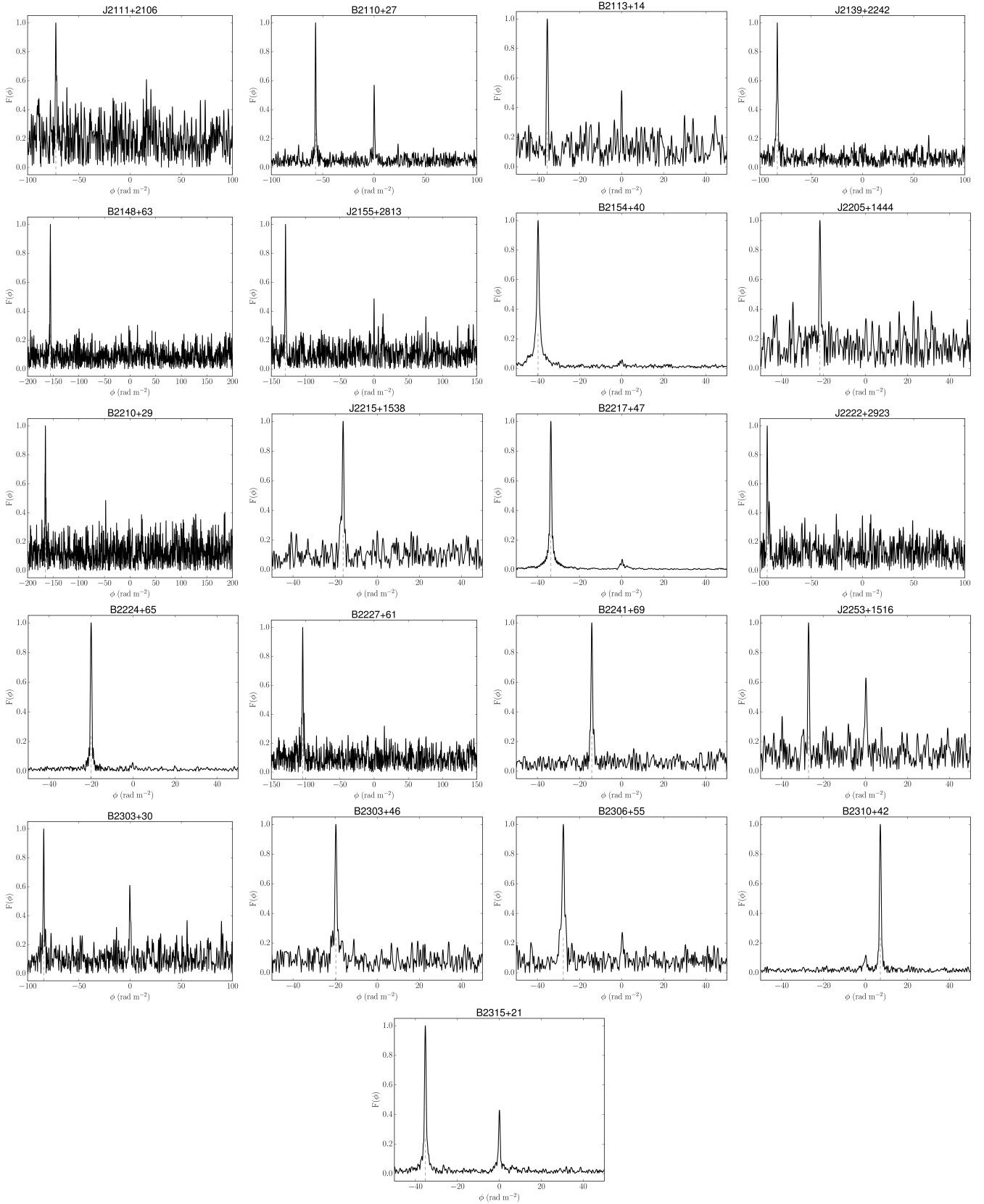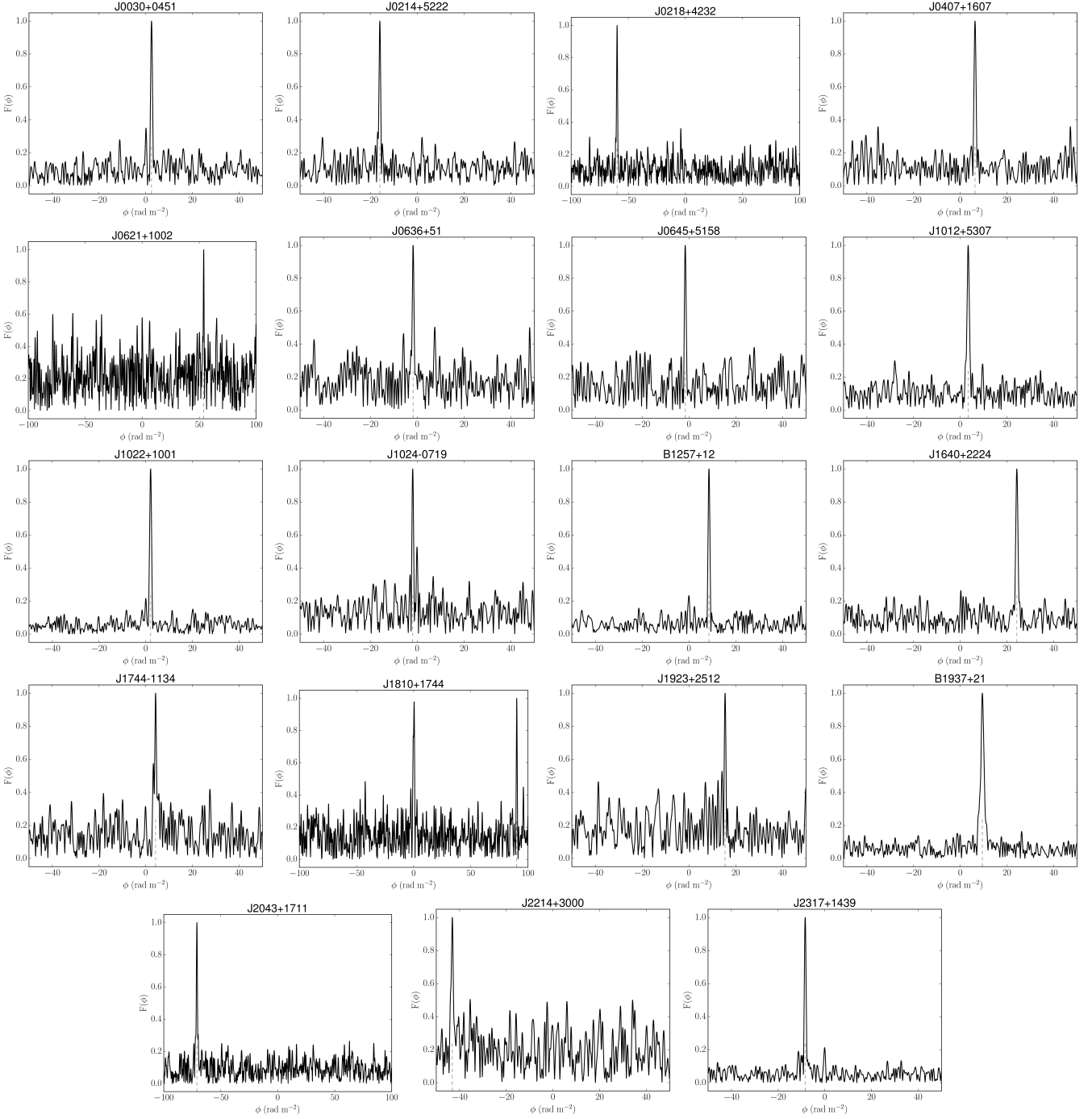**Figure B6.** Continued from the previous page.

Figure B7. Continued from the previous page.

Figure B8. Continued from the previous page.